A Semi-Analytical Model for Prior Strain in Ballistically Perforated Steel Plates

Graduation Thesis

Katie Moyano

Student Name	Student Number
Katie Moyano	5738237

Thesis Advisor:	Dr. C.L. Walters, TU Delft
Company Representative:	Ir. O. Coppejans, TNO
Defense Committee:	Prof. Dr. M. Veljkovic, Dr. C.L. Walter, W. J. Wong, Ir. O. Coppejans
Faculty:	ME Marine Technology

TU Delft

Abstract

High-strength marine grade steel is often used in naval applications where ballistic impact poses a critical threat to structural integrity. Perforation by a projectile leaves behind a hole surrounded by plastically deformed material, which alters the stress redistribution capacity of the impacted structural component and reduces its residual strength. Understanding and predicting these effects is essential for reliable damage assessment and safe structural design.

This work develops a semi-analytical stress field model for perforated EH36 steel plates that incorporates prestrain effects derived from Vickers hardness measurements around ballistic holes. The model builds upon Stowell's elastoplastic stress concentration framework, extended with a Swift-type hardening law to capture strain hardening from prior plastic deformation.

The analytical solution results are compared with finite element analysis (FEA) and limited experimental Digital Image Correlation (DIC) data. While the validation dataset is not sufficient for full generalization, the comparisons indicate that incorporating prestrain reduces the stress concentration factor at the edge of the hole compared to analyses without prior strain.

Contents

List of Figures

List of Tables

Nomenclature

Abbreviations

Abbreviation	Definition
CHT	Central Hole Test
DIC	Digital Image Correlation
EBSD	Electron Backscatter Diffraction
FEA	Finite Element Analysis
FEM	Finite Element Modeling
XRD	X-Ray Diffraction

Symbols

Symbol	Definition	Unit
A	Saturation hardening parameter (Voce)	[MPa]
a	Perforation radius	[mm]
E	Young's modulus	[MPa]
E_s	Secant modulus	[MPa]
$E_{s,\text{loc}}$	Local secant modulus	[MPa]
$E_{s,\infty}$	Far-field secant modulus at σ_∞	[MPa]
F	Force	[N]
G	Shear modulus	[MPa]
H_V	Vickers hardness	
K	Strength coefficient (Hollomon)	[MPa]
k_{pr}	Prestrain distribution fitting parameter	-
k_s	Strength coefficient (Swift law)	[MPa]
n	Strain hardening exponent (Hollomon, Swift)	-
r	Radial distance from center of perforation	[mm]
r/a	Normalized radius	–
x, y	Coordinates	[mm]
ε	Strain	-
ε_0	Initial strain	-
$\varepsilon_{L,1}$	First Principal Lagrange Strain	-
ε_l	Local strain	-
$\varepsilon_{pr,max}$	Maximum prestrain at hole	-
ε_{pl}	Plastic strain	-
ε_{pr}	Prior plastic strain or prestrain	-
ν	Poisson's ratio	-
ρ	Density	[kg/m^3]
σ	Stress	[MPa]
σ_∞	Stress applied far from discontinuity	[MPa]
σ_θ	Hoop stress	[MPa]
σ_{1-3}	Principal stresses	[MPa]
σ_l	Local stress	[MPa]
σ_r	Radial stress	[MPa]
σ_{vM}	Von-Mises stress	[MPa]
σ_y	Yield stress	[MPa]

Symbol	Definition	Unit
θ	Angular location	[rad]
$\tau_{r\theta}$	Shear stress	[MPa]

1

Introduction

When a projectile such as a bullet, missile, or fragment strikes a steel plate, its kinetic energy is transferred into the plate primarily through mechanical work. This transfer manifests as plastic deformation, perforation, and fracture, and may be exacerbated by subsequent blast loading. This thesis aims to expand traditional plate models to incorporate the effects of ballistic impact material damage in the form of altered material properties. Including these effects in the plate model will increase understanding of the structure's ability to withstand post-impact loading.

Such failures are particularly critical in marine and defense structures. It is especially relevant for naval defense applications due to the larger risk of encountering ballistic impact. An example of a critical structural member in ships is the bulkheads, providing transverse and longitudinal support necessary for withstanding the dynamic loading conditions encountered at sea, in addition to the separation of vital areas and equipment and flooding confinement. Maintaining the separation of critical compartments prevents explosion damage from compromising the vessel's structure and hydrodynamic stability. Ensuring the structural integrity of these elements is crucial for safeguarding human lives and reducing economic loss in the event of an attack.

Due to the risks and consequences associated with the failure of ship bulkheads, quantifying the effects of damage due to ballistic impact is of high interest. Part of the challenge in capturing these mechanisms and their subsequent effect on the material's structural response is their complex nature. While finite element analysis methods (FEA) are commonly used to model ballistic damage, they are computationally expensive. Analytical models offer an efficient alternative, but traditional methods, such as Kirsch's solution for stress fields around a hole, do not consider plasticity effects. Stowell's approach modifies the elastic solution by incorporating a secant modulus correction for plasticity, but it does not explicitly include pre-existing damage or plasticity. While Swift's hardening law accounts for prior strain, its direct integration into Stowell's model for prestrain-induced stress redistribution has not been explicitly established in existing work.

This thesis develops a prestrain enhanced stress field model for perforated high-strength steel plates. By integrating experimental Vickers hardness measurements and a Swift-style hardening law, it refines stress redistribution predictions.

2

Literature Review

This section outlines the theoretical concepts that underpin the modelling of steel plates with ballistic perforation damage under subsequent loading and existing relevant research.

2.1. Damage

Ballistic impact leads to complex material degradation involving void nucleation, shear banding, and microcracking. These phenomena are often captured through micromechanical or continuum damage models (e.g., GTN, MMC, HC) that track evolving damage variables to predict failure. However, such models are computationally intensive and require extensive calibration. In this work, damage is treated implicitly via residual plastic strain and strain hardening around the perforation, estimated using hardness measurements. This approach enables an efficient semi-analytical formulation that captures the effect of prior damage without explicitly modeling void growth or fracture surfaces.

The interest in the topic of damage extends over many fields and physical scales. With respect to material and structural behavior, the definition of the scale is necessary. Figure 2.1 illustrates the scale categories for the general topic of material damage study. This thesis' focus is the effect of damage on the macro scale. ”Damage” here refers to the breaking of a once continuous plate via the mechanism of plate perforation from high velocity impact. The perforated plate is assumed to fail at the moment crack initiation is observed at the perforation.

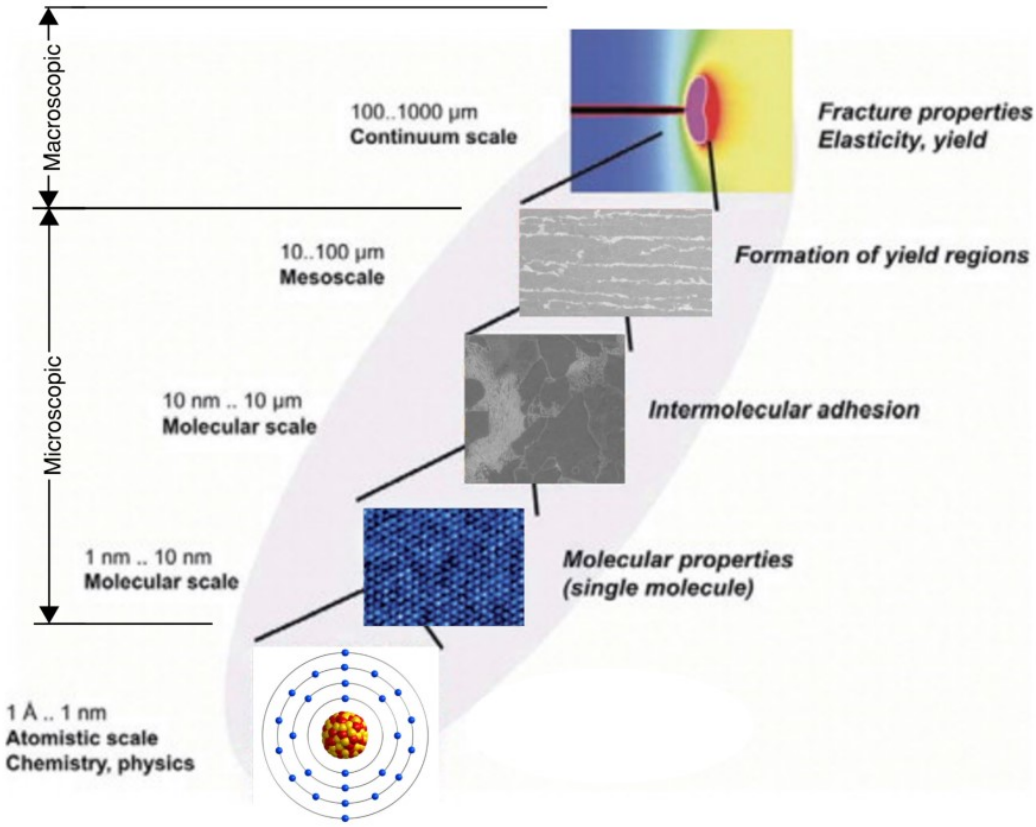

Figure 2.1: Overview of different material scales [2]

2.1.1. Ballistic Induced Damage

Plate Perforation

Perforation in this context refers to the full penetration of a stationary plate by a high velocity projectile, where the projectile impacts the front face, goes through the plate and exits completely through the plate. The failure mechanisms induced on the plate by the projectile's impact can include spalling, discing, and plugging due to the large shearing that occurs, [24]. The type and extent of this failure depends on the projectile's shape, velocity, angle of impact, and material properties, in addition to the thickness and material properties of the plate being impacted. If the plate is thin (with an approximate ratio of plate thickness to projectile diameter less than one), stretching and bending could also occur, [24]. Often, a combination of failure mechanisms will occur in a plate perforation. Figure 2.2 is an example of plate perforation by plugging.

Plugging occurs as a result of the plastic shear deformation due to the high velocity of the projectile's impact with the plate. A narrow ring of localized plastic shear and thermal softening is formed around the perimeter of the projectile, [25]. This band of material around the hole has modified properties from the original base material due to the re-crystallization that occurs. The exact form of re-crystallization depends on the base steel's microstructure. The behavior of a plate with a perforation due to plugging shear failure is of interest in this thesis work.

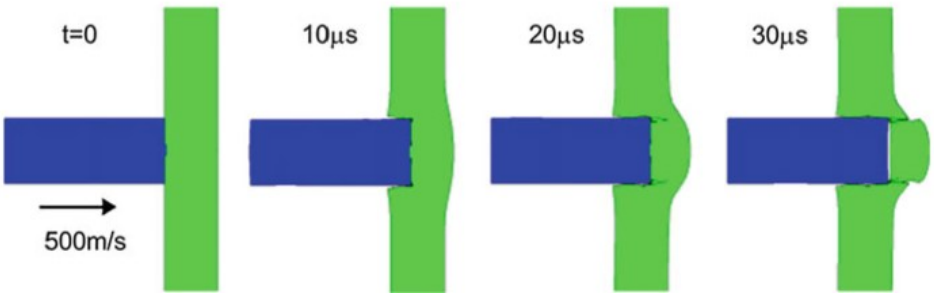

Figure 2.2: Example of plate perforation, [24]

The ring of localized plastic shear and thermal softening around the perforation at high strain rates (greater than $10^2\ s^{-1}$ [18]) is often associated with the formation of adiabatic shear bands (ASBs) [24]. These bands are narrow zones where high amounts of plastic deformation occur due to localized thermal effects. ASBs form when thermal energy, generated from the conversion of mechanical energy (such as from a projectile impact), causes localized slip and further heating. Due to the large strain rate, the heat generated cannot dissipate fast enough, exacerbating the deformation [22]. These bands reduce the material's ductility and can lead to the initiation and propagation of cracks. A material's likelihood to develop ASBs and the amount of ASBs formed is a factor of its heat capacity, amount of defects, thermal conductivity, strength, microstructure, and geometry [12].

2.2. Strain Hardening

Ballistic perforation of steel plates introduces large, localized plastic strains at high strain rates (typically in the range of 1850-3600 s^{-1}), followed by a blast-induced pressure load at lower strain rates (on the order of 100 s^{-1}). During the impact, the material surrounding the projectile path undergoes rapid plastic deformation, resulting in a strain-hardened zone around the perforation. In this region, the material exhibits increased yield strength and decreased ductility due to accumulated dislocation density.

Although strain rate sensitivity strongly influences material behavior during the impact event, this project focuses on the post-impact (quasi-static) response of the plate — particularly how the residual strain and hardening affect the strain at the time of crack initiation at the edge of the perforation. For this reason, dynamic constitutive models such as Johnson–Cook [10], Cowper–Symonds [5], or Zerilli–Armstrong [32], which include explicit strain rate terms, are not employed here. Instead, the residual plastic deformation from the high strain rate event is treated as a modified material state in the vicinity of the hole, characterized by increased flow stress and altered hardening behavior.

Strain hardening is incorporated into the stress field model through empirical relationships such as Hollomon's or Swift's laws, which relate flow stress to plastic strain under monotonic loading. These models enable the definition of a non-linear stress–strain response that reflects the hardened state of the material after perforation. In this work, Vickers hardness measurements near the hole are used to infer the local yield strength and plastic strain, providing an experimental basis for defining the pre-strained material zone. This approach aims to capture the effect of the strain-hardened shell around the hole on the stress redistribution and the far-field failure strain during subsequent tensile loading.

2.3. Multiaxial Yielding

A yield criterion defines the onset of plastic deformation in multiaxial stress states and must be used in conjunction with a hardening law to capture post-yield behavior. Since the material is assumed to be isotropic and experiences monotonic loading, anisotropic or kinematic effects such as directional hardening, cyclic response, or the Bauschinger effect are outside the scope of this work.

The von Mises yield criterion ([14]) predicts the onset of yielding in isotropic, ductile materials. Yielding occurs when the second deviatoric stress invariant reaches a critical value, which is independent of hydrostatic stress. It is relevant for ductile materials that exhibit elastic-perfectly-plastic behavior in

addition to materials that have experienced strain hardening, [6], [24].

While this work does not explicitly implement a yielding criterion in the analytical formulation, the use of Stowell's stress redistribution model implicitly assumes von Mises yielding. Additionally, an upper limit on the stress field calculations is defined to avoid non-physically realistic magnitudes. In the numerical simulations, von Mises is used as the default yield criterion in Abaqus, with yielding defined based on experimental tensile data.

2.4. Elasticity & Plasticity

The material model used in this thesis follows classical assumptions of isotropic, rate-independent plasticity under quasi-static loading. Although the ballistic impact involves high strain rates, this work focuses exclusively on the post-impact behavior, where deformation occurs slowly and strain rate sensitivity can be neglected.

The foundational assumptions are:

- Plasticity is isotropic and follows monotonic loading.
- Thermal effects, creep, and time-dependent recovery are negligible.
- Material behavior is spatially uniform far from the perforation and modified near the hole by pre-strain.
- Kinematic hardening and Bauschinger effects are not considered.

2.4.1. Plastic Deformation and Hardening

Hardening describes how a material's resistance to plastic deformation evolves after yielding. In this work, isotropic hardening is assumed, consistent with monotonic loading and the absence of cyclic or directional effects.

Isotropic hardening refers to a uniform expansion of the yield surface in all directions within the stress space, representing a material's increased ability to sustain higher stress without yielding as it undergoes plastic deformation, [30]. Unlike kinematic hardening, isotropic hardening does not consider directional changes but assumes that the material hardens equally in all stress directions.

Kinematic hardening describes how the yield surface of a material translates in the stress space as the material undergoes cyclic loading. This model assumes that the center of the yield surface moves in the stress space, but stays the same size as the original yield surface, [30]. Figure 2.3 demonstrates the difference between isotropic and kinematic hardening. An isotropic hardening model will be used in this project.

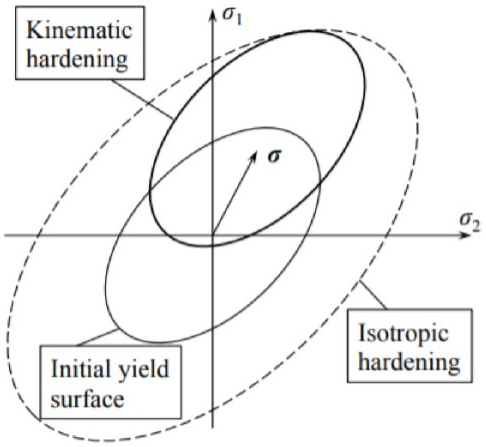

Figure 2.3: Isotropic vs kinematic hardening under plane stress [30]

2.5. Relating Hardness to Stress and Strain

Vickers hardness is a common deformation resistance measurement for metals, using a square based diamond indenter with high hardness. A force is applied to the indenter, creating an impression on the surface of the softer material. The size of the impression is measured optically. The resultant Vickers hardness measurement is calculated using the average of the diagonals and the applied force. Pavlina and Van Tyne studied the correlation between diamond pyramid hardness (Vickers) and the yield and tensile strength of more than 150 steels, finding a linear correlation for all studied steels, [19]. Hirano et al. [7] developed a relationship between Vickers hardness and elastic-plastic material constants. This was done with finite element analysis and validated against experimental results for various metals including steels, copper, aluminum alloys, and titanium alloys. They found that Vickers hardness increases with increasing yield stress and strain hardening coefficient, but decreases with increasing strain hardening exponent. Based on their simulations, they proposed an explicit functional equation relating Vickers hardness to the yield stress, strain hardening coefficient, and strain hardening exponent

2.6. Existing Work

This section provides an overview of relevant models, approaches, and research used to understand and predict material behavior related to hardening, deformation, and failure under high velocity impact, and the subsequent material response.

2.7. Models

To capture the behavior of deformed steel damaged by high velocity impact, both empirical and analytical models are employed. The work in this thesis will use and modify relevant models to define a constitutive relationship for the material behavior model of a finite plate with ballistic perforation. Figure 2.4 outlines the relationship between the types of models that will be discussed in this section.

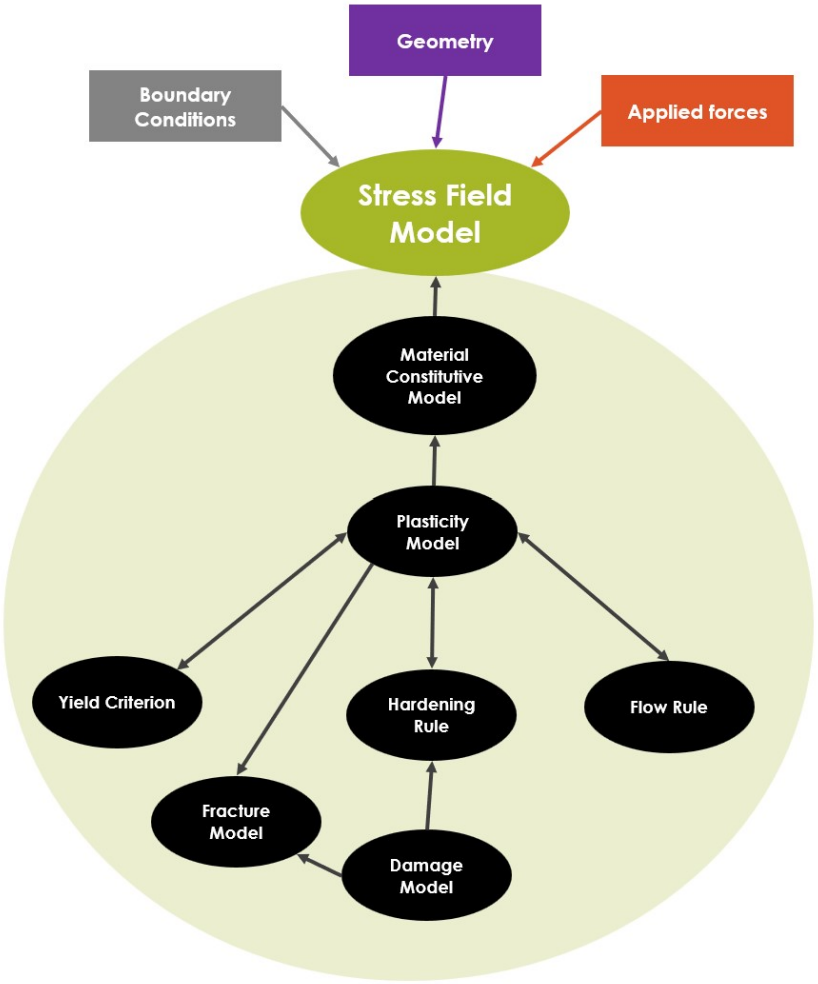

Figure 2.4: Overarching model relationships

2.7.1. Hardening

Hardening models describe how the yield surface of a material expands once plastic hardening begins. The relationships described in this section are candidates for use in this thesis' modeling efforts.

Hollomon

Hollomon's power law [8] [16] is a commonly used equation for the relationship between strain and stress when material hardening is present. The Hollomon equation has advantages due to its simplicity, and is independent of strain rate.

$$\sigma = K \cdot \varepsilon^n \tag{2.1}$$

Swift

The Swift hardening law [28] extends Hollomon's power law, often used in metal forming processes to model strain hardening. It introduces a pre-strain term to account for initial plastic deformation:

$$\sigma = K \left(\varepsilon_0 + \varepsilon\right)^n \tag{2.2}$$

2.7.2. Stress Field - Circular Cutouts

Kirsch - Elastic Solution

Kirsch's solution [11] [1] is a classical linear elastic analytical solution for the stress field around a circular hole in an isotropic plate subjected to uniaxial tension. The solution is derived under the assumption that

the plate is infinite and the hole is small relative to the dimensions of the plate. Governing equilibrium equations:

$$\frac{\partial \sigma_x}{\partial x} + \frac{\partial \tau_{xy}}{\partial y} = 0, \frac{\partial \sigma_y}{\partial y} + \frac{\partial \tau_{xy}}{\partial x} = 0 \tag{2.3}$$

Using the Airy stress function, ϕ, stress components are expressed as:

$$\sigma_x = \frac{\partial^2 \phi}{\partial y^2}, \quad \sigma_y = \frac{\partial^2 \phi}{\partial x^2}, \quad \tau_{xy} = -\frac{\partial^2 \phi}{\partial x \partial y} \tag{2.4}$$

The stress function must satisfy the biharmonic equation in polar coordinates:

$$\nabla^4 \phi = \left(\frac{\partial^4}{\partial r^4} + \frac{2}{r^2}\frac{\partial^3}{\partial r^3} - \frac{1}{r^2}\frac{\partial^2}{\partial r^2} + \frac{1}{r^3}\frac{\partial}{\partial r} + \frac{1}{r^4}\frac{\partial^4}{\partial \theta^4} \right) \phi = 0 \tag{2.5}$$

Using separation of variables, the Airy stress function becomes:

$$\phi = Ar^2 + Br^4 + Cr^2 \cos 2\theta + Dr^4 \cos 2\theta \tag{2.6}$$

Where Ar^2 and Br^4 correspond to the uniform far-field stresses and $Cr^2 cos2\theta$ and $Dr^4 cos2\theta$ account for the stress concentration effects from the hole. Application of boundary conditions at the hole (2.7) and far-field (2.8) allow for the unknown constants to be solved for, resulting in Kirsch's final stress system (2.10, 2.9, 2.11).

Hole edge boundary condition:

$$\sigma_r(a, \theta) = 0, \quad \tau_{r\theta}(a, \theta) = 0 \tag{2.7}$$

Far-field boundary condition:

$$\sigma_r \to \sigma_\infty, \quad \sigma_\theta \to \sigma_\infty, \quad \tau_{r\theta} \to 0 \tag{2.8}$$

Resulting stress system:

$$\sigma_r = \frac{\sigma}{2}\left[1 - \frac{a^2}{r^2} + \left(1 + 3\frac{a^4}{r^4} - 4\frac{a^2}{r^2}\right)\cos 2\theta\right] \tag{2.9}$$

$$\sigma_\theta = \frac{\sigma}{2}\left[1 + \frac{a^2}{r^2} - \left(1 + 3\frac{a^4}{r^4}\right)\cos 2\theta\right] \tag{2.10}$$

$$\tau_{r\theta} = -\frac{\sigma}{2}\left(1 - 3\frac{a^4}{r^4} + 2\frac{a^2}{r^2}\right)\sin 2\theta \tag{2.11}$$

The resulting stress concentration factor (K_t) for this approach is approximately 3, indicating that the stress at the edge of the hole is about three times the applied stress. This solution is fundamental in understanding the baseline stress distribution around holes in materials and serves as a starting point for more complex analyses.

Stowell - Elastic-Plastic Correction

Stowell's approach [27] extends Kirsch's solution to include the plastic stress reduction that occurs due to the stress redistribution around the hole. The key contribution of Stowell's work is its ability to describe how stress redistributes when a material transitions from elastic to plastic behavior around stress concentrations, such as notches or holes. He does this using the stress concentration relationship, 2.12, that relies on the ratio of the maximum, local secant modulus and the far field secant modulus to account for the stress redistribution. Stowell satisfies the boundary conditions because the ratio $\frac{E_s}{(E_s)_\infty}$ goes to 1 at infinity (resulting in the stress system going back to the original elastic solution), and at the hole $\frac{E_s}{(E_s)_\infty}$ goes to 0.

$$1 + 2\frac{(E_s)_{a,\pi/2}}{(E_s)_\infty} \tag{2.12}$$

The stresses become:

$$\sigma_r = \frac{\sigma}{2}\left[1 - \frac{a^2}{r^2} + \frac{E_s}{(E_s)_\infty}\left(1 + 3\frac{a^4}{r^4} - 4\frac{a^2}{r^2}\right)\cos 2\theta\right] \tag{2.13}$$

$$\sigma_\theta = \frac{\sigma}{2}\left[1 + \frac{a^2}{r^2} - \frac{E_s}{(E_s)_\infty}\left(1 + 3\frac{a^4}{r^4}\right)\cos 2\theta\right] \tag{2.14}$$

$$\tau_{r\theta} = -\frac{\sigma}{2}\frac{E_s}{(E_s)_\infty}\left(1 - 3\frac{a^4}{r^4} + 2\frac{a^2}{r^2}\right)\sin 2\theta \tag{2.15}$$

The governing equations in Stowell's method are derived based on the assumption of a plane stress condition and small plastic zones around the notch. For the elastic region, the stress components are given by Kirsch's classical solution. As plastic deformation occurs, the stress distribution is modified to reflect strain hardening effects. Stowell's method is implicit and requires an iterative solution method.

Obers - Yield Ratio Model

In this work, the relationship developed by Obers between the secant modulus E_s and Hollomon's power law is used, 2.17. Obers [17] developed a relationship between the yield to tensile strength ratio and stress field in high-strength steel, specifically a plate with a circular cutout. This was done with an analytical model using Stowell's applied method and Neuber's approximation, combined with Irwin's plastic zone size estimation and Stowell's local strain equation. Hollomon's law was used to describe plasticity, and the results were numerically validated using FEA.

Using Hollomon's law:

$$\sigma_{\text{true}} = K\varepsilon_{\text{true}}^n \tag{2.16}$$

The secant modulus E_s is given by:

$$E_s = \frac{\sigma_{\text{true}}}{\varepsilon_{\text{true}}} = K\varepsilon_{\text{true}}^{n-1} \tag{2.17}$$

2.7.3. Elastic to Plastic Transition Models

Neuber

Neuber's rule [15] was originally developed for elastic-plastic stress concentrations, particularly in shear-strained prismatic bodies, but it can be generalized to arbitrary nonlinear stress-strain relationships. It is primarily used to analyze stress and strain concentrations at notches or geometric discontinuities. The rule establishes the relationship between stress and strain concentration factors by assuming that the product of local stress and strain remains consistent between elastic and elastic-plastic conditions. This is interpreted as ensuring that the strain energy density in the elastoplastic state is equal to that in a pseudo-elastic state. This method can be useful in incorporating stress-strain relationships into the strain field.

$$K_\sigma K_\varepsilon = K_{\sigma,el}^2 \tag{2.18}$$

$$\sigma_{eq}\varepsilon_{eq} = \sigma_{el}\varepsilon_{el} \tag{2.19}$$

While this work does not directly apply Neuber's pointwise energy balance rule, it shares conceptual similarity by estimating elastoplastic stress redistribution using an adjusted elastic solution combined with nonlinear hardening behavior. Like Neuber, this approach modifies classical elastic predictions to account for local plastic deformation, but does so over a spatially varying field rather than at a single point.

2.8. Existing Research

2.8.1. Microstructural Level

Understanding the microstructural characteristics of the material under impact can provide important insight into the mechanisms that lead to the mechanisms of strain hardening and void formation that lead to visible failure modes. In the context of this thesis, which focuses on high-strength structural steels (e.g., EH36), such insights help justify the presence and profile of a prestrained zone around a ballistic perforation. Kouzoudis et al [13] conducted microstructural analysis of EH36 TM and N specimens using techniques such as scanning electron microscopy, energy dispersive spectroscopy, and electron backscatter diffraction. These investigations were performed across the three principal planes of the material—rolling direction, transverse direction, and normal direction [13]. Additionally, Kouzoudis' master thesis [12] estimated the geometric limits of the plasticity and measures the hardness values in both through thickness direction and radially on the specimen surface in multiple locations on the perforated samples. This work provides essential data for the current thesis' prestrain modeling approach.

2.8.2. Continuum Level

At the macrostructural plate level, multiple solutions have been developed to model and solve for the stress field behavior of a plate with various boundary, loading, and discontinuity configurations.

Ballistic Perforation

Riegel [23] investigated penetration modeling using empirical, analytical, and numerical approaches. The empirical data relied on the Effective Flow Stress model, which was applied in the analytical Walker-Anderson penetration model. This flow stress value can also serve as an effective von Mises yield strength in numerical hydrocode simulations to predict penetration depth for eroding projectiles. Riegel's study questions the applicability of the Johnson-Cook model in terminal ballistics problems, advocating for a more integrated approach using empirical, analytical, and numerical methods.

Moreover, Mandal et al. (2022) employed high-performance computing (HPC) techniques, such as GPU-accelerated FEA, to simulate dynamic failure in armor plates. These simulations offer more detailed and efficient models of complex failure modes. While this thesis does not simulate the perforation event itself, such studies inform boundary assumptions and validate strain localization patterns in post-impact modeling.

Plate with Discontinuity

Obers [17] investigated the relationship between the yield to tensile strength ratio and stress field in high strength steel, specifically a plate with a circular cutout. This was done using Stowell's [27] and Neuber's [15] methods, with Irwin's [9] stress field analogy. Hollomon's law [8] was used to describe plasticity, and the results were numerically validated with FEA. Although this work focused on cleanly machined holes, the mathematical framework is relevant for adapting to ballistically-induced, prestrained holes, as done in this thesis.

Additional research, such as that by Yu and Liu [31], has advanced the study of stress fields around discontinuities by implementing extended finite element methods (XFEM) and generalized finite element method (GFEM). This combination enhances accuracy in stress analysis near discontinuities by employing generalized node shape functions around cracks while using conventional finite element shape functions elsewhere. While not used in this thesis, these studies validate the need for non-classical approaches when modeling highly localized plastic zones — such as those around projectile holes.

Another key area of relevance is the study of prestrain history effects on ductile fracture in high-strength steels. Zhang et al. [33] investigated how different levels of prestrain influence the fracture behavior of pipeline steels. Their work showed that the fracture strain is significantly reduced in regions subjected to prior plastic deformation, and that the stress state at failure is also altered by the prestrain history. Using both experimental and finite element analyses, they established that materials with higher prestrain exhibit earlier fracture initiation and reduced ductility, even under similar loading conditions. These findings are particularly relevant for this thesis, as they highlight how residual plastic deformation from ballistic impact can influence subsequent failure modes. While Zhang et al. focused on pipeline applications, the underlying principle — that strain history modifies the material's local resistance to fracture — directly supports the need to include prestrain fields in stress field models for perforated plates.

2.8.3. Global Structural Level

Prior-Damage

Global-scale studies of damaged ships provide valuable context for structural integrity post-impact. Prabowo [21] incorporated damage-induced plasticity into global FEA models of ship structures to evaluate collapse thresholds. Chen et al. [4] and Storheim et al. [26] also modeled large-scale collision responses in marine structures, highlighting the structural impact of local plastic damage.

Additional work by Pije [20] proposed a failure model for a bulkhead subjected to fragment damage from projectile impact using a plate model. Pije employed equivalent plastic strain to account for the accumulation of plastic deformation, incorporating a semi-local failure model that linked the stress state around the hole's edge to the equivalent plastic strain at fracture initiation. This work considered three levels of detail (global, semi-local, and local), modeling the undamaged material around the hole but accounting for damage through a reduction in the admissible equivalent plastic strain at failure. Pre-existing microcracks and surface imperfections were assumed to be included in the reduction. This study noted that more investigation is required to fully understand the role of prior damage in fracture initiation.

Although this thesis does not operate at the full-ship level, these studies reinforce the importance of incorporating prior local damage into structural assessments — especially when localized events (like ballistic impact) can affect far-field behavior.

2.9. Research Gap

Existing research that has explored material behavior under high-strain-rate loading and post-impact structural responses of perforated plates include:

- Microstructural studies have investigated and documented changes in crystalline structure for EH36 steel incurred by ballistic impact, [12].
- Analytical stress field models (Kirsch, Stowell, Neuber, Obers) predict stress concentrations around discontinuities, in a plate of a uniform material.
- Hardening models (Hollomon, Swift) describe material strengthening post-deformation but have not been extensively integrated into stress field analyses for prestrained perforated plates.

However, these models have key limitations:

- Kirsch's elasticity solution does not account for plastic deformation.
- Stowell's correction accounts for stress redistribution in the plastic zone but does not explicitly incorporate prestrain effects.
- Obers' study links the yield-to-tensile ratio to stress concentrations but assumes uniform material properties and does not include the effects of prior plastic deformation.
- Numerical (FEA) models can capture detailed stress-strain behavior, including plasticity and damage, but are computationally intensive and not ideal for rapid assessment or generalization.

The redistribution of stress and strain in a perforated plate with prestrain history remains inadequately described. Ballistic perforation induces a plastic zone near the hole, altering the yield strength, ductility, and subsequent stress concentration during loading. This zone often exhibits material hardening and reduced deformability, which classical models fail to account for.

Despite the integration of Hollomon's hardening model into Stowell's stress concentration approach, existing models still lack direct incorporation of prestrain effects from ballistic perforation. This is critical because the initial impact often induces significant plastic deformation, resulting in spatially varying material properties around the perforation. The current research aims to begin to bridge this gap by developing a model that explicitly incorporates prestrain effects while leveraging the enhanced stress-strain relationship enabled by Hollomon's law. The model will be validated using both experimental data and numerical simulations to ensure accuracy and robustness.

2.10. Steel Data

This study uses experimental data from EH36 steel specimens to inform the development and validation of the analytical and numerical models. The chemical composition of the EH36 steel used is shown in Table 2.1. EH36 was selected due to its widespread use in marine structures and availability of detailed microstructural and mechanical property evaluations for both the base steel and perforated samples, providing additional insight into pre and post perforation conditions of the steel. Both the non-perforated and perforated specimens underwent tensile and central hole (CHT) tests with digital image correlation (DIC) analysis, in addition to XRD, Vickers hardness, electron backscatter diffraction (EBSD), and fractography measurements [12].

Table 2.1: EH36 chemical composition, [12]

Chemical Composition	Fe	C	Mn	Si	S	P	Cr	N	Ni	Cu	Al	Ti	Mo	Nb	V	**CE**
Manufacturer [mass%]	bal	0.14	1.5	0.5	0.001	0.01	0.04	0.004	0.06	0.3	0.07	0.003	0.03	0.01	0.001	**0.40**
XRF and Leco [mass%]	98.17	0.14	1.23	0.46	0.004	-	0.04	-	-	0.3	0.07	-	0.02	0.01	-	-
Abs error [%]	0.5	0.002	0.06	0.01	0.0004	0.003	0.01	-	-	0.01	-	-	-	0.004	-	-

To quantify strain hardening effects caused by the ballistic impact, Vickers hardness measurements were taken radially outward from the hole edge at 0.5 mm intervals, Table 2.2. Vickers hardness is calculated using the applied force and the contact area of the indentor. The indentation at the location of maximum hardness near the perforation is shown in Figure 2.5. The aim of these measurements was to evaluate hardness gradients and identify potential work-hardening effects resulting from the ballistic perforation. The hardness data revealed a localized hardened zone, consistent with plastic deformation gradients expected from high-velocity impact, Figure 2.6.

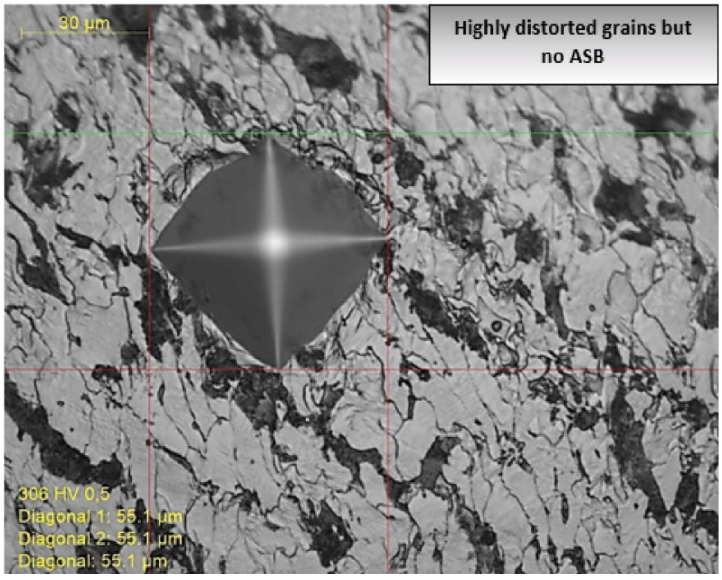

Figure 2.5: Vickers microhardness indentations at maximum hardness value, [12]

The Vickers hardness number (H_V) is given by the formula, [3]:

$$H_V = \frac{2F \sin\left(\frac{2\theta}{2}\right)}{d^2}$$

Where:

- H_V = Vickers hardness (kgf/mm^2)
- F = Applied load (kgf)
- θ = Angle between opposite faces of the diamond indenter (136°)

- d = Average diagonal length of the indentation (mm)

By simplifying the formula with $\theta = 136°$, we obtain:

$$H_V = \frac{1.8544 \cdot F}{d^2}$$

Vickers hardness can be empirically related to the yield strength through a proportionality constant. The general empirical relationship is given by:

$$\sigma_y \approx \frac{H_V}{3} \tag{2.20}$$

This relationship holds because the hardness value is a measure of the resistance of the material to plastic deformation. The factor of 3 arises from the geometric relationship between the indenter and the material's flow stress. The hardness value can therefore be interpreted as an approximate indicator of the material's ability to withstand permanent deformation under load, [29].

Table 2.2: Hardness measurements at different X-distances from edge of perforation, [12]

X Location of Measurement (mm)	Hardness (kgf/mm^2)
0.48	290
1.00	261
1.50	248
2.00	248
2.50	229
3.00	210
3.50	215
4.00	226
4.50	215
5.00	217
5.49	220.
6.00	212
6.49	207
6.99	218
7.50	202
8.00	203
8.48	179
8.98	186
9.50	178
10.0	188
10.5	177
11.0	172
11.5	172
12.0	173
12.5	180
13.0	182
13.5	178
14.0	173
14.5	168
15.0	163
15.5	169

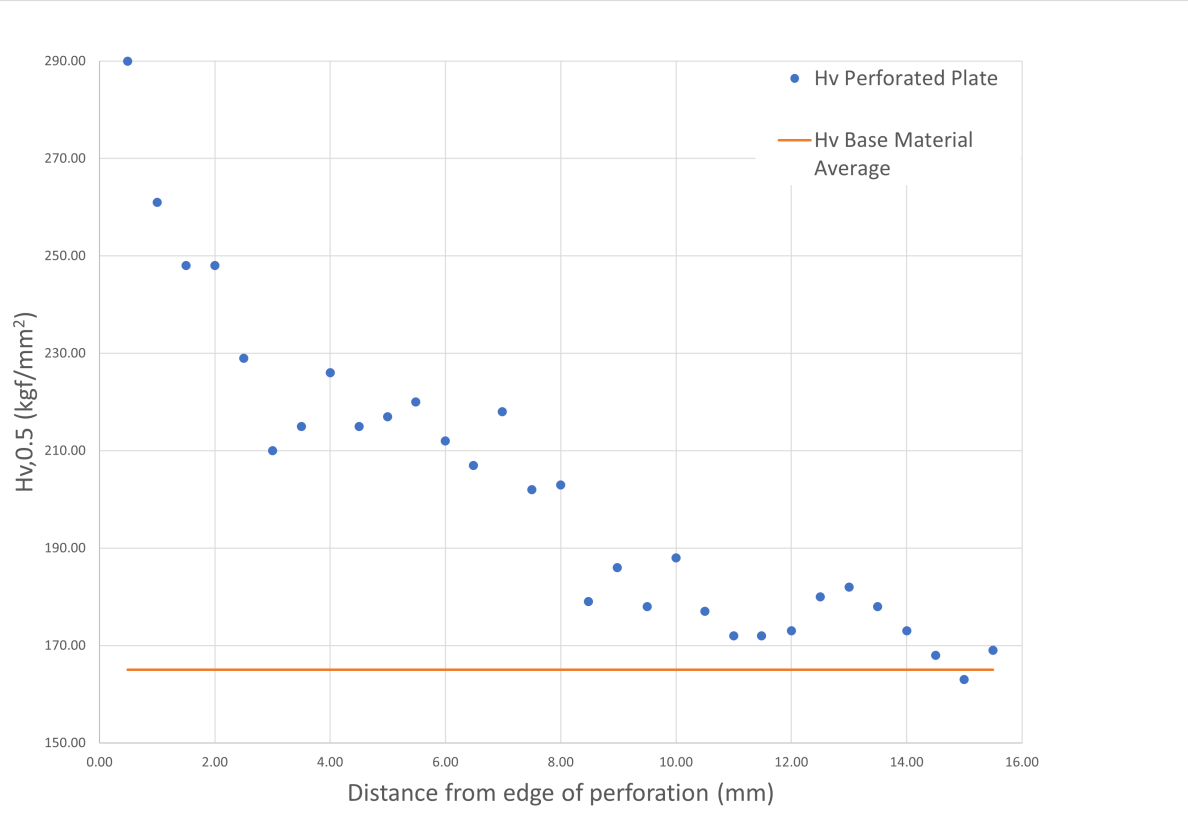

Figure 2.6: Hv measurements at x locations on perforated plate surface, [12]

Tensile tests were performed on both non-perforated and perforated specimens to characterize the material's elastic and plastic response under uniaxial loading, Figures 2.7 and 2.8. Non-perforated tests established baseline values for the elastic modulus, yield stress, and ultimate tensile strength. Perforated specimens were used to investigate the influence of prior plastic deformation around the hole on far-field strain response. During testing of the perforated specimens, digital image correlation (DIC) was used to capture strain fields at the time of crack initiation at the edge of the hole, Figure .

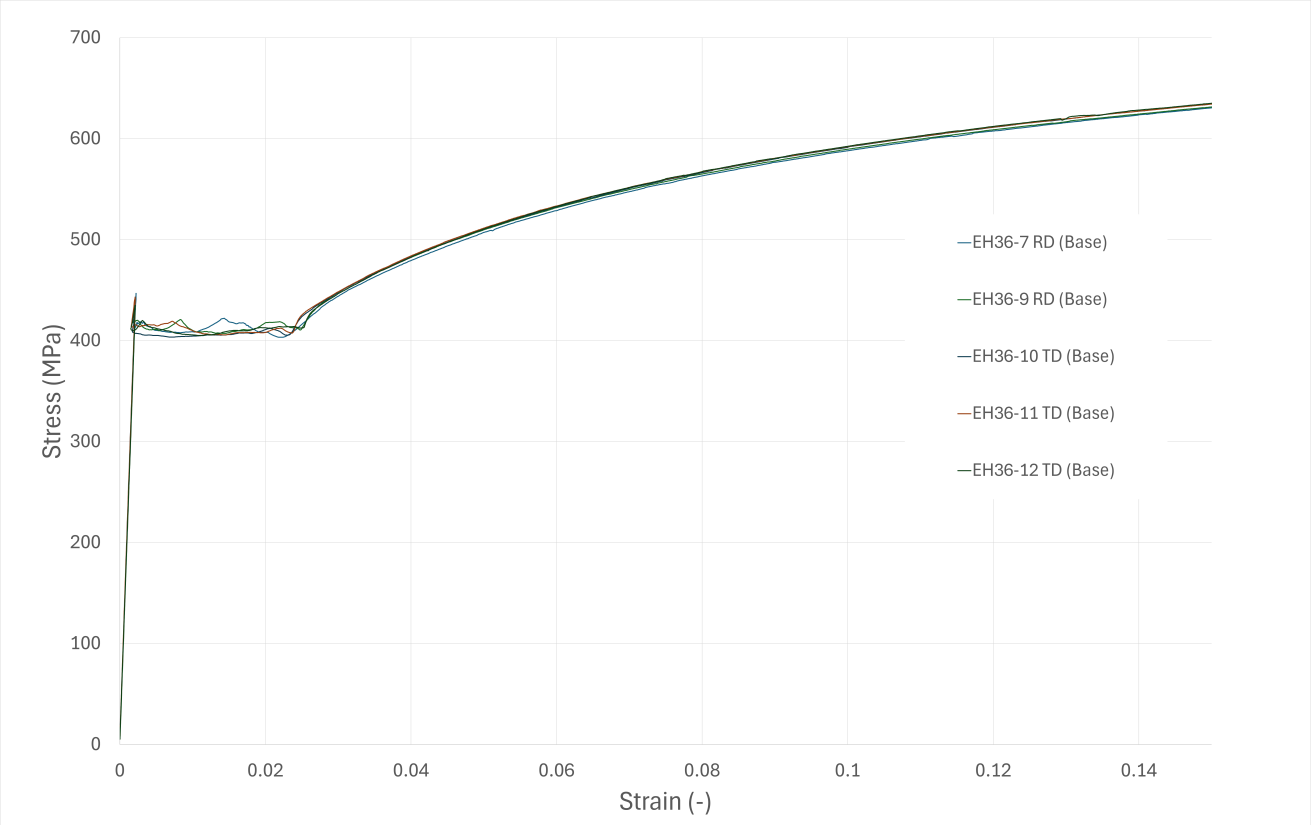

Figure 2.7: EH36 base steel tensile test, courtesy of TNO

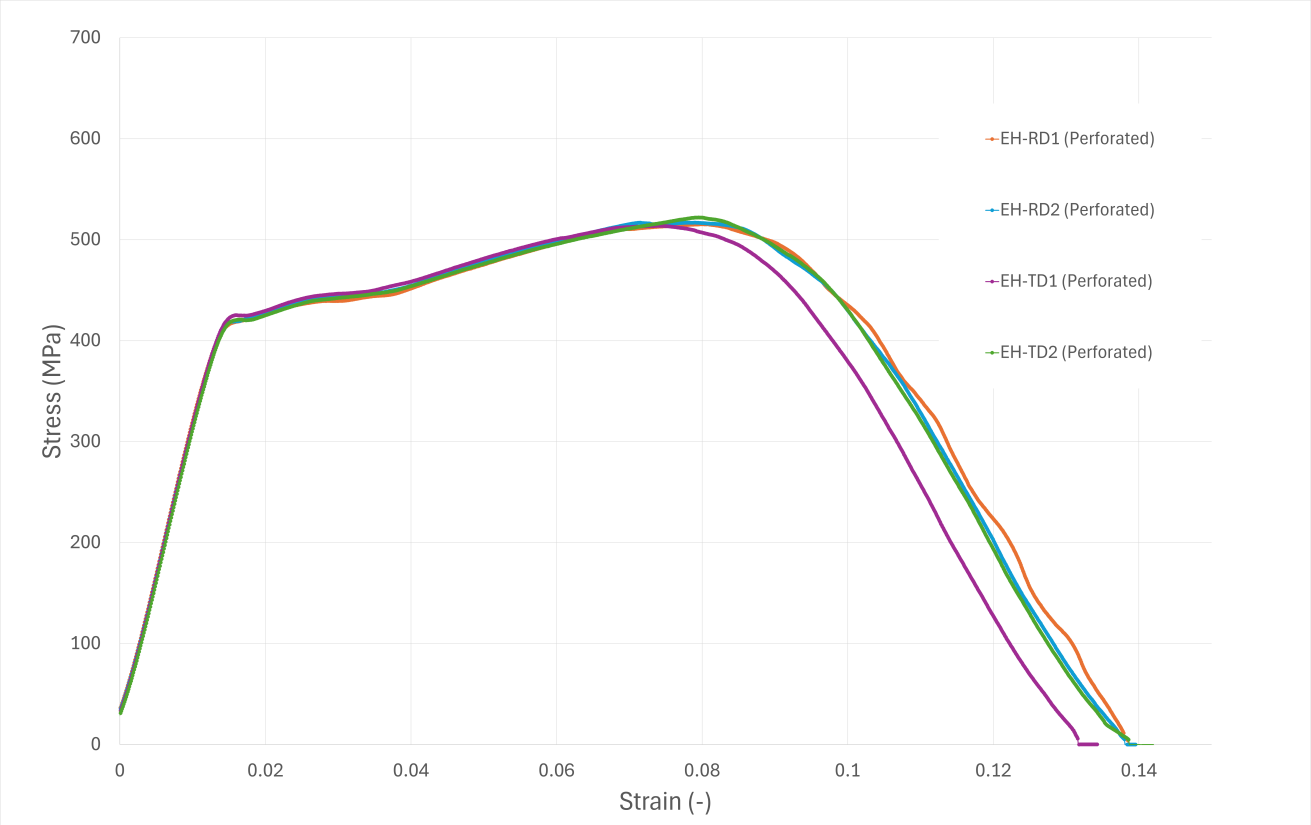

Figure 2.8: EH36 perforated plate tensile test, courtesy of TNO

Figure 2.9: Close up of perforation cross section post fracture, courtesy of TNO

3

Research Question

The central research question for this project is:

What is the influence of ballistic impact-induced prestrain on the stress concentration factor (SCF) in EH36 steel plates?

Sub questions that will need to be answered in order to support the central research question are:

- *Does modeling the prior damage by estimating the prestrain induced by the initial projectile impact compare well with experimental data and numerical methods?*
- *Can available hardness measurements be used to determine reliable prestrain estimates and material properties in the zone of plastic deformation around the perforation?*

4

Approach and Scope

This chapter outlines the methodological framework for the thesis, detailing the scope of the research, the development process for the model, and the validation process.

4.1. Scope

The localized damage and prestrain from ballistic perforation is incorporated into the Stowell stress system using a Hollomon-Swift style hardening law. Stowell's stress system incorporates a correction factor into Kirsch's solution to account for the plastic field. In order to model prior plastic strain's affect on the stress field of the plate, a function for the prestrain is determined using hardness data from the perforated specimen. The model accounts for the non-zero initial strain in the steel plate, specifically around the perforation, as a result of the plastic deformation induced by the impact. This prestrain serves as the starting condition for estimating the stress-strain curves of the material in the vicinity of the perforation. The stress field around the perforation is modeled considering these non-zero strain values at various radial distances from the damage site. A geometrical zone of plastic behavior is delineated using available data. The stress field in the vicinity of the perforation is then be related to the far-field stress field of the plate.

4.2. Material Model and Prestrain Incorporation

The localized plastic deformation caused by projectile impact introduces a nonzero initial strain field. To incorporate this, a version of Hollomon's isotropic hardening law with a strain shift (prestrain) is used. The prestrain is estimated using hardness measurements of the damaged steel specimens. This will serve as the starting condition for the stress-strain analysis of the perforated plate. Vickers Hardness data is used to quantify the prestrain at varying radial distance from the hole. The material hardening model will employ isotropic hardening.

4.3. Stress Field Modeling

This approach adapts the analytical stress field models to account for the spatially varying strain history around the perforation. This includes implementing:

- Empirical hardness-strain relationships to establish an initial strain profile
- Modifications to Stowell's model to reflect the redistribution of stress due to pre-existing plastic deformation
- Analytical prediction comparisons with experimental data to ensure consistency

4.4. Assumptions

The following assumptions are adopted for modeling:

- The material is isotropic and follows isotropic hardening; plane-stress plate response with negligible through-thickness variation.
- Strain rate effects from the ballistic impact are neglected; post-impact loading is treated as quasi-static.
- Kinematic hardening and Bauschinger effects are not considered.
- Far from the perforation, the material properties are spatially uniform.
- Temperature effects, creep, and time-dependent recovery are ignored.

4.5. Validation Strategy

Validation and model verification will be performed through a combination of numerical and experimental approaches:

- Finite Element Analysis (FEA): A numerical model will be developed using Abaqus CAE, incorporating spatially varying material properties around the perforation.
- Experimental Data Comparison: Digital Image Correlation (DIC) measurements from uniaxial tensile tests on perforated specimens, provided by TNO, will be used to benchmark the numerical and analytical results.

The experimental data provided by TNO was utilized to calibrate and validate the analytical and numerical work. The DIC of the perforated specimens undergoing uniaxial tensile tests were compared to the strains calculated from the analytical and FEA model.

5

Semi-Analytical Approach

This chapter presents the development of a modified analytical stress field model that incorporates prestrain effects resulting from ballistic perforation. The model builds upon Stowell's classical plastic correction approach, modified to include a prestrain field derived from empirical Vickers hardness data around the perforation. The geometrical layout and loading direction of this model is shown in Figure 5.1, where the color gradient represents the zone with existing damaged material or the zone of prior plastic strain.

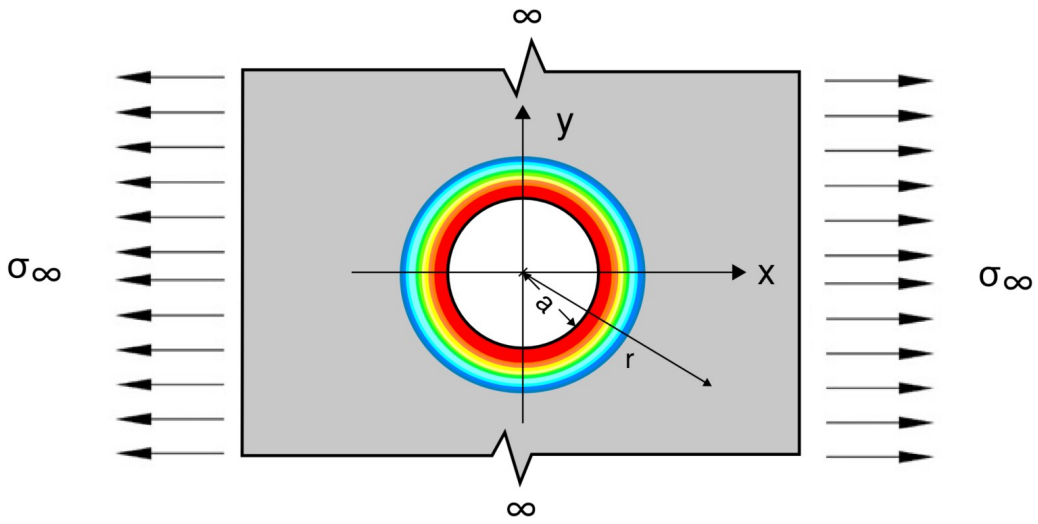

Figure 5.1: Loading convention

5.1. Prior Plastic Strain Field

The local strain is decomposed into two components: the residual plastic strain from the ballistic impact (prestrain), and the strain due to subsequent applied far-field loading. The local strain in the system is estimated as a summation of the prior plastic strain and subsequent plastic strain. The plastic strain is estimated using Hollomon's:

$$\varepsilon_{pl} = \left(\frac{\sigma_{pl}}{K}\right)^{\frac{1}{n}} \tag{5.1}$$

The prior plastic strain field is given by an exponentially decreasing function found from curve fitting the prestrain distribution from the Vickers Hardness measurements:

$$\varepsilon_{pr} = \varepsilon_{pr,max} \cdot e^{-k_{pr}\left(\frac{r}{a}-1\right)} \tag{5.2}$$

where:

- $\varepsilon_{pr,max}$ is the maximum prestrain near the hole found from the Vickers Hardness measurements,
- r is the distance from the center of the hole,
- k_{pr} is the fitting parameter,
- a is the hole radius.

Leading to the total local strain summation:

$$\varepsilon_l = \varepsilon_{pl} + \varepsilon_{pr} \tag{5.3}$$

5.1.1. Strain from Vickers Hardness

The maximum prestrain value is the strain at the corresponding stress value calculated from the relationship with Vickers Hardness and defined by the stress-strain function of the tensile test specimens. For example, the maximum Vickers Hardness measurement taken on the EH36 sample is approximately 290 kg/mm^2, or 2844 MPa, resulting in a corresponding yield stress of 770 MPa if Equation 5.5 is used. The average Vickers hardness of the base material and the documented yield strength of the base material were used to find a more accurate relationship between Hv and yield strength (both in MPa).

$$\frac{H_{v,avg,EH36}}{\sigma_{y,EH36}} = \frac{1618.7}{438} = 3.7 \tag{5.4}$$

Equation 5.4 becomes:

$$\sigma_y \approx \frac{H_v}{3.7} \tag{5.5}$$

The value of strain corresponding to the maximum Vickers hardness at the edge of the perforation is calculated from the Hollomon relationship using the average of the material fit parameters from testing, Table 5.1. This yields an approximate maximum strain value of 0.4 at the edge of the perforation.

Table 5.1: Hollomon fit data, TNO

	K (MPa)	**n**
43053-1A-EH36-Trans-NoFailure	919.6	0.2
43053-1B-EH36-Trans-NoFailure	889.8	0.2
43053-2A-EH36-Long-NoFailure	937.5	0.2
43053-2B-EH36-Long-NoFailure	940.8	0.2
Averages:	**921.9**	**0.2**

The resulting prestrain distribution using Equation 5.2 and the maximum prestrain value results in the distribution in Figure 5.2. The curve fitting parameter, k_{pr}, is found using a Nelder-Mead simplex optimization method. The resultant fitted curve is compared to the Hollomon strain curve, which represents the strain calculated using Hollomon's with the stresses found from the Vickers measurements along the x direction from the edge of the perforation.

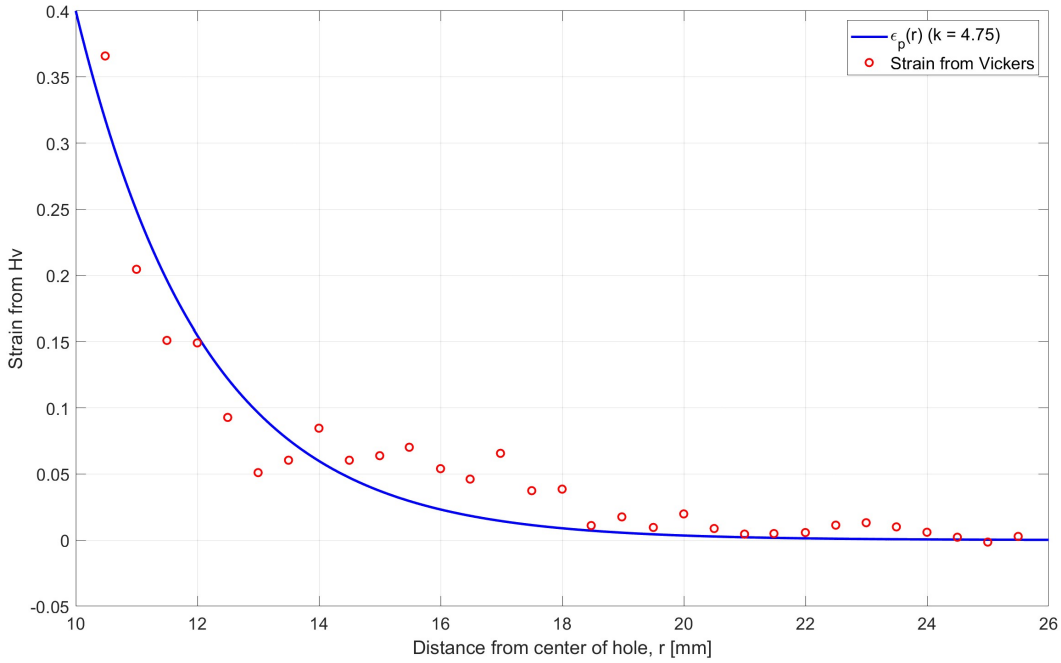

Figure 5.2: Prestrain distribution from hardness data

5.2. Implicit Solution Method

Figure 5.3 outlines the method for solving the system of equations for the final local stress values.

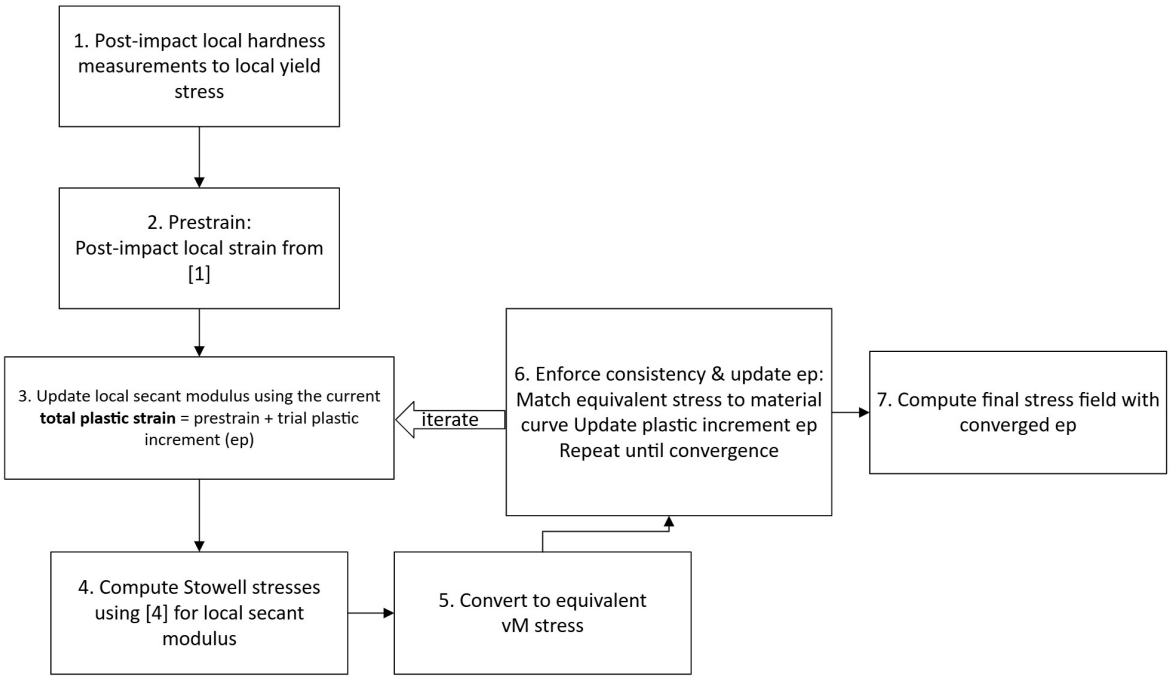

Figure 5.3: Solution process

Input For each point (r, θ), remote stress σ_∞, hole radius a, Young's modulus E, Hollomon parameters (K, n), prestrain $\varepsilon_{p0}(r) \geq 0$, and far-field secant modulus $E_{s,\infty}$.

Unknown The incremental equivalent plastic strain $\varepsilon_p \geq 0$ such that the local stress state is self-consistent with the material law.

Local secant modulus. Define the local flow stress from Hollomon (true stress)

$$\sigma_{\text{flow}}(\kappa) = K\,\kappa^{\,n}, \qquad \kappa := \varepsilon_{p0} + \varepsilon_p, \tag{5.6}$$

$$\varepsilon_{\text{tot}}(\kappa) = \underbrace{\frac{\sigma_{\text{flow}}(\kappa)}{E}}_{\text{elastic true strain}} + \underbrace{\kappa}_{\text{plastic (equiv.)}}, \tag{5.7}$$

$$E_s(\kappa) = \frac{\sigma_{\text{flow}}(\kappa)}{\varepsilon_{\text{tot}}(\kappa)}. \tag{5.8}$$

Stowell stress field (plane stress) Let $c_2 = \cos(2\theta)$, $s_2 = \sin(2\theta)$, $\rho = (a/r)^2$, and $\phi(\kappa) := E_s(\kappa)/E_{s,\infty}$. The Stowell stresses at (r, θ) are

$$\sigma_\theta(r,\theta;\kappa) = \tfrac{1}{2}\,\sigma_\infty\big[\,1 + \rho \;-\; \phi(\kappa)\,\big(1 + 3\rho^2\big)\,c_2\big]\,, \tag{5.9}$$

$$\sigma_r(r,\theta;\kappa) = \tfrac{1}{2}\,\sigma_\infty\big[\,1 - \rho \;+\; \phi(\kappa)\,\big(1 - 4\rho + 3\rho^2\big)\,c_2\big]\,, \tag{5.10}$$

$$\tau_{r\theta}(r,\theta;\kappa) = -\tfrac{1}{2}\,\sigma_\infty\,\phi(\kappa)\,\big(1 + 2\rho - 3\rho^2\big)\,s_2. \tag{5.11}$$

Von Mises equivalent stress (plane stress)

$$\sigma_{\text{vm}}(r,\theta;\kappa) = \sqrt{\sigma_r^2 - \sigma_r\sigma_\theta + \sigma_\theta^2 + 3\,\tau_{r\theta}^2}\;. \tag{5.12}$$

Consistency enforcement Solve for $\varepsilon_p \geq 0$ (equivalently for $\kappa = \varepsilon_{p0} + \varepsilon_p$) such that

$$f(\varepsilon_p) \;:=\; \sigma_{\text{vm}}\big(r,\theta;\,\kappa\big) \;-\; \sigma_{\text{flow}}(\kappa) \;=\; 0. \tag{5.13}$$

Secant update Given two iterates $\varepsilon_p^{(k-1)}, \varepsilon_p^{(k)}$ with residuals $f^{(k-1)} = f(\varepsilon_p^{(k-1)})$, $f^{(k)} = f(\varepsilon_p^{(k)})$, update via

$$\varepsilon_p^{(k+1)} = \max\Big\{\,0,\; \varepsilon_p^{(k)} \;-\; f^{(k)}\;\frac{\varepsilon_p^{(k)} - \varepsilon_p^{(k-1)}}{f^{(k)} - f^{(k-1)}}\Big\}, \tag{5.14}$$

until a stopping criterion holds, e.g.

$$|f^{(k+1)}| < \text{tol}_F \quad \text{or} \quad \big|\varepsilon_p^{(k+1)} - \varepsilon_p^{(k)}\big| < \text{tolerance}. \tag{5.15}$$

Output At convergence, set $\varepsilon_p^\star(r,\theta) = \varepsilon_p$ and report the local fields

$$E_s^\star(r,\theta) = E_s\big(\varepsilon_{p0} + \varepsilon_p^\star\big), \tag{5.16}$$

$$\boldsymbol{\sigma}^\star(r,\theta) = \big(\sigma_r, \sigma_\theta, \tau_{r\theta}\big) \text{ evaluated at } \kappa = \varepsilon_{p0} + \varepsilon_p^\star, \tag{5.17}$$

$$\sigma_{\text{vm}}^\star(r,\theta) = \sigma_{\text{vm}}\big(r,\theta;\,\varepsilon_{p0} + \varepsilon_p^\star\big). \tag{5.18}$$

The stress field and equivalent von Mises stress are then recomputed with the converged ε_p.

6

Numerical Approach

6.1. Models

To investigate the effects of material and geometric variations on stress and strain distributions, the following model versions were developed:

- Baseline Model: A perforated plate with uniform material properties, serving as a reference case for subsequent modifications.
- Variable Material Properties Model: A perforated plate incorporating a spatially varying material definition, representing strain hardening effects induced by ballistic perforation. This variation was included to account for prestrain effects and material property changes in the vicinity of the hole.

Simulations were carried out using Abaqus/CAE, version 2024, developed by Dassault Systèmes Simulia Corp.

6.1.1. Geometry

To maximize computational efficiency while maintaining accuracy, the perforated plate was modeled three-dimensionally, but only one-quarter of the plate was included in the simulations. This approach leverages the geometric symmetry of the problem, reducing computational costs while still capturing the relevant stress and strain distributions. To compare to the analytical solution, thee simulation with prestrain was performed with plate boundaries far from the location of the hole to simulate an infinite plate. Three-dimensional, solid continuum elements (C3D8R) were used.

6.1.2. Boundary Conditions

The applied boundary conditions enforced symmetry along the relevant planes, constraining displacement at the vertical and horizontal symmetry planes while allowing deformation in the positive X direction at the edge of applied load, Figure 6.1. The loading was applied as a uniform tension at the remote boundary, simulating a far-field tensile stress condition. The simulations were carried out using the standard implicit solver.

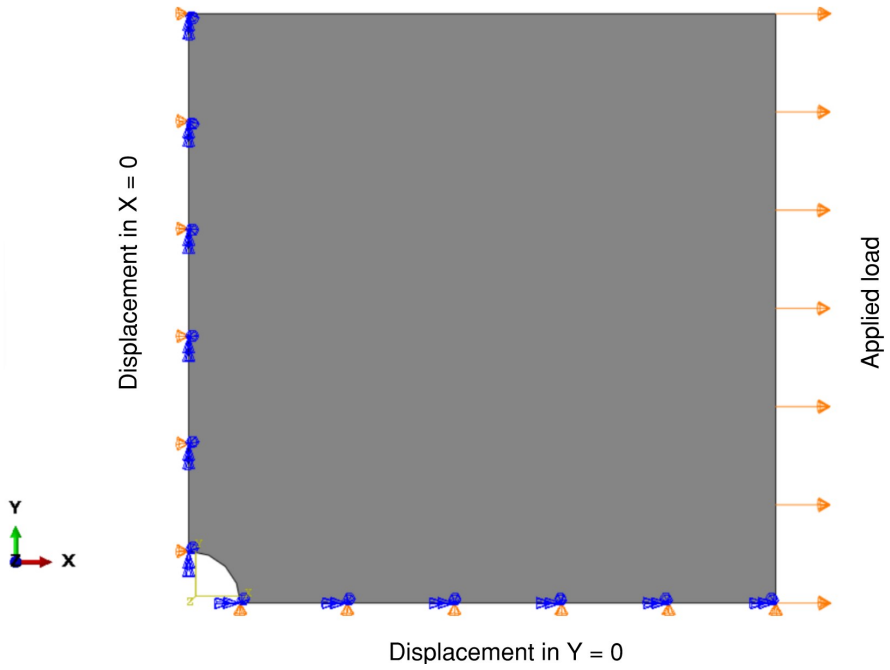

Figure 6.1: Plate boundary conditions

6.2. Material Calibration

To achieve accurate material representation in the finite element simulations, material properties were calibrated against experimental data. The base material was defined using an isotropic linear elastic material model, with properties specified by Young's modulus and Poisson's ratio from tensile testing of non-perforated EH36 specimens.

For simulations incorporating the effects of prior plastic deformation near the ballistic perforation, an elasto-plastic material definition was applied. The stress strain curves of the plastic material zones were determined from the radially varying prestrain field around the hole. The Vickers hardness measurement data were fitted to obtain a smooth equivalent prestrain profile, then a Swift law was used to build a local true stress versus effective plastic strain curve for the FEA material definitions. This was done for each radial point from the perforation that Vickers hardness measurements were collected. These radially-dependent curves were assigned as discrete field-dependent plasticity material definitions in the FEA. The discrete field links node locations to the corresponding stress–strain curves based on their radial distance from the perforation. The nodes outside the zone of prior plastically hardened material are assigned the base material (not prestrained) properties. In this way, the simulation starts from the pre-damaged state (via the shifted curves) and evolves additional plasticity consistently during loading.

Because the discrete field definitions are assigned at the nodes, the material behavior at the elements in Abaqus is interpolated from the stress–strain curves associated with the element's corner nodes. Abaqus evaluates the material properties at each integration point by interpolating the field variable(s) from the nodal values using the element's shape functions. This means that if different nodes of a single element are linked to different stress–strain curves, the resulting behavior within that element will reflect a weighted average of those curves across the integration points. While this introduces a level of approximation, it still allows the model to capture smooth transitions in mechanical behavior across the strain-hardened zone and reasonably represents the material heterogeneity surrounding the hole. For elements located at the boundary of two or more material zones, this averaging enables a gradual transition rather than an abrupt material jump, which helps mitigate numerical instabilities while still preserving the physical gradients.

6.3. Mesh Convergence

A mesh convergence study was conducted to ensure that the finite element results were independent of mesh density and adequately captured the stress gradients around the perforation. The mesh was progressively refined in regions of high stress concentration, at the location of maximum stress near the edge of the hole, where accurate resolution of the strain-hardened material behavior is more critical.

Convergence was assessed by monitoring the maximum von Mises stress at the location of maximum stress. Since the mesh was not uniformly refined for the entire plate, the mesh size directly at and surrounding the perforation was used. Multiple mesh configurations were tested, and the maximum von Mises stress at the edge of the perforation was recorded for each to identify when further refinement resulted in negligible change. To further improve efficiency, variable mesh sizing was applied, using finer elements near the perforation and coarser elements in regions of low stress gradients. This allowed for improved computational performance without sacrificing accuracy in the critical area.

The results demonstrated convergence in the maximum von Mises stress values beyond a minimum mesh seed size at the hole of 1 mm, indicating that the solution was mesh-independent.

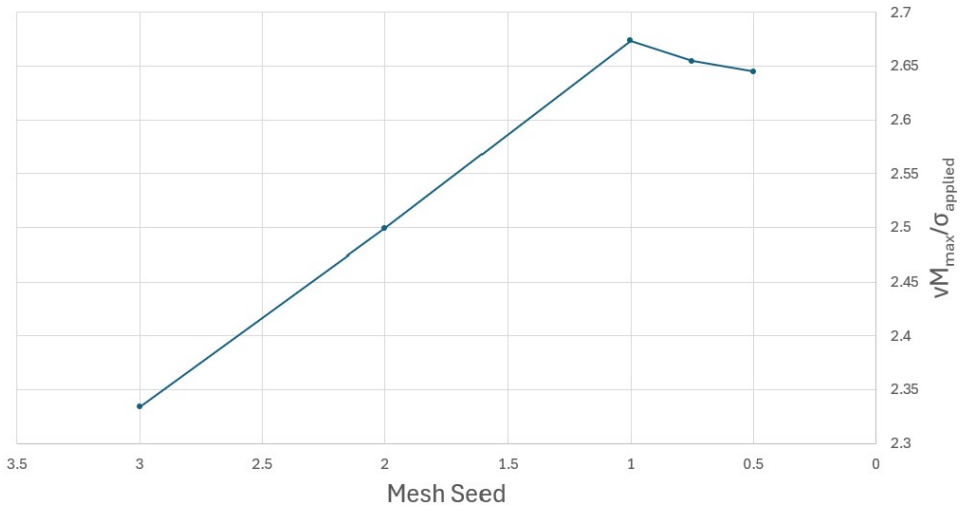

Figure 6.2: Mesh convergence

7

Results

The following sections discuss the results of the analytical and numerical method results, the validation efforts and parametric study performed.

7.1. Semi-Analytical

Figure 7.1 shows the resultant stress concentration contours for one quadrant of the plate. The model assumed an infinite plate geometry (no edge effects) but the results are plotted to a limited r/a.

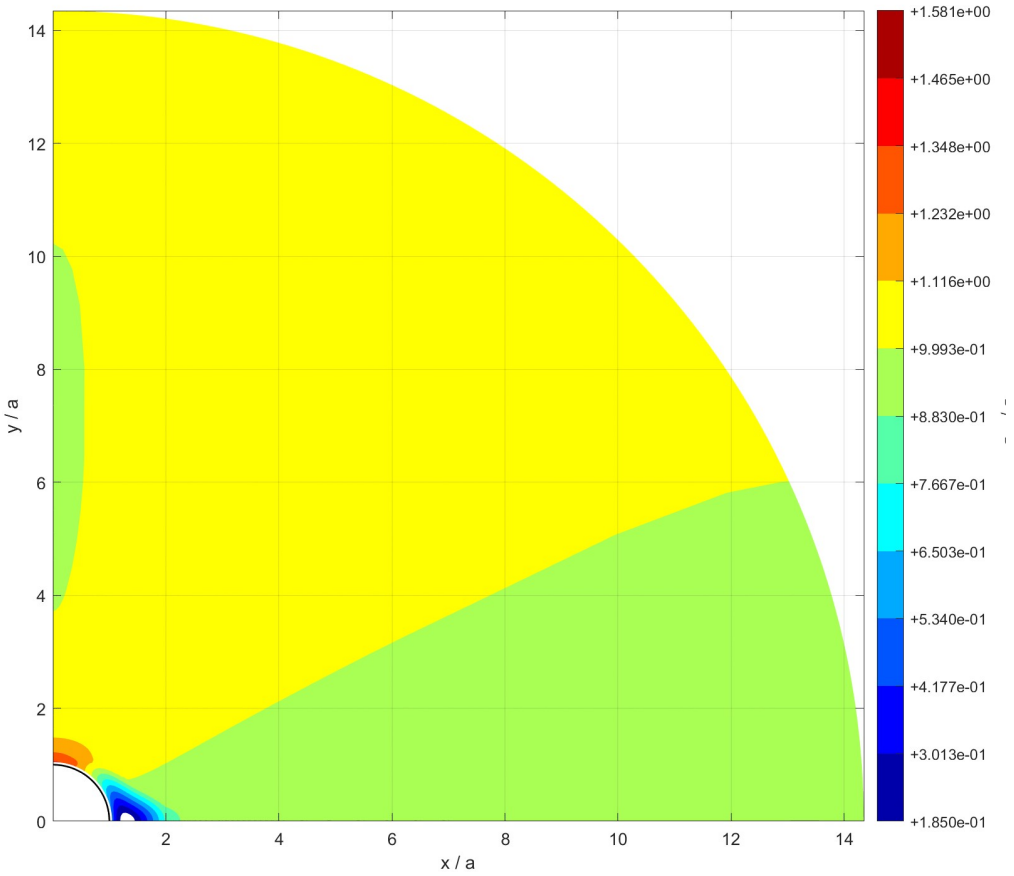

Figure 7.1: von Mises SCF analytical model with prestrain - applied stress 481 MPa

7.2. Numerical

The results of the numerical simulations for the plate with base material properties and varying material properties presented in this section. Figure 7.2 and 7.3 show the SCF of the von Mises stress for the model without prestrain incorporation and with prestrain incorporation respectively.

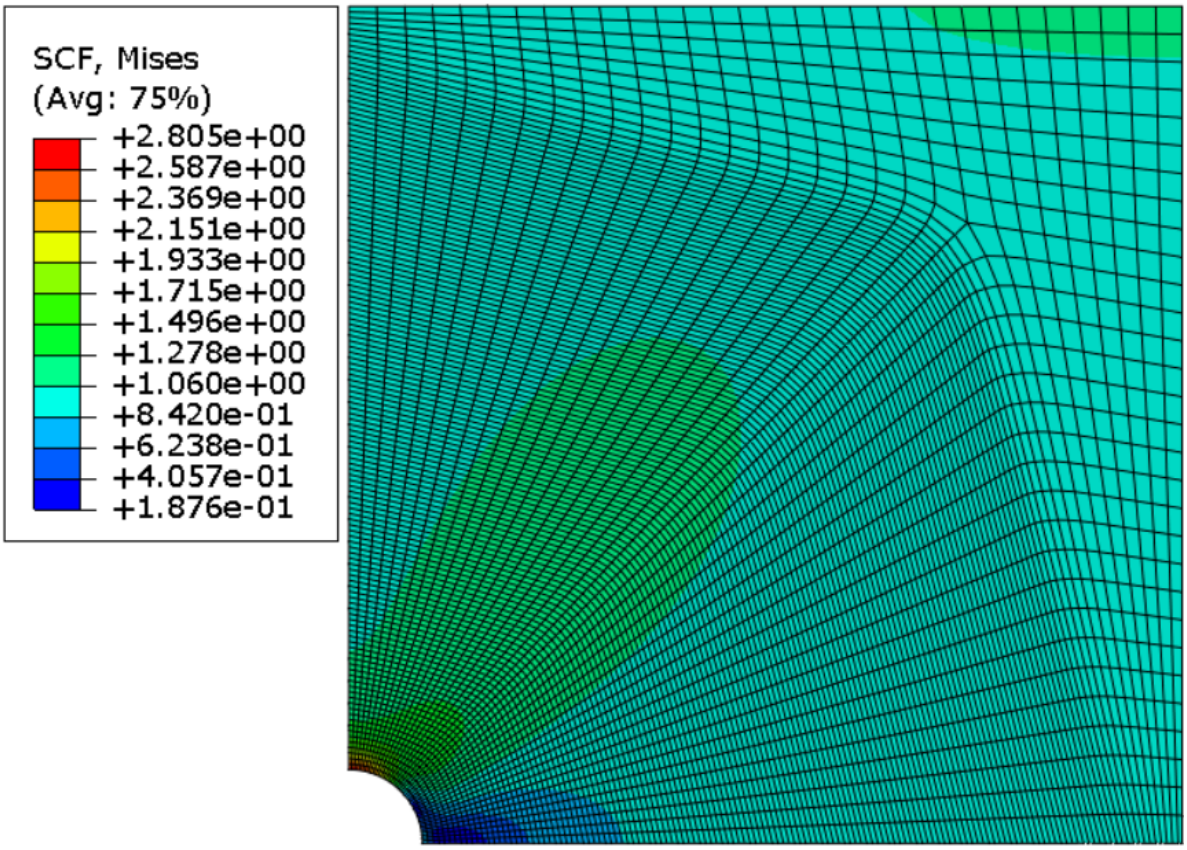

Figure 7.2: von Mises SCF for plate with elastic material definition - applied stress 481 MPa

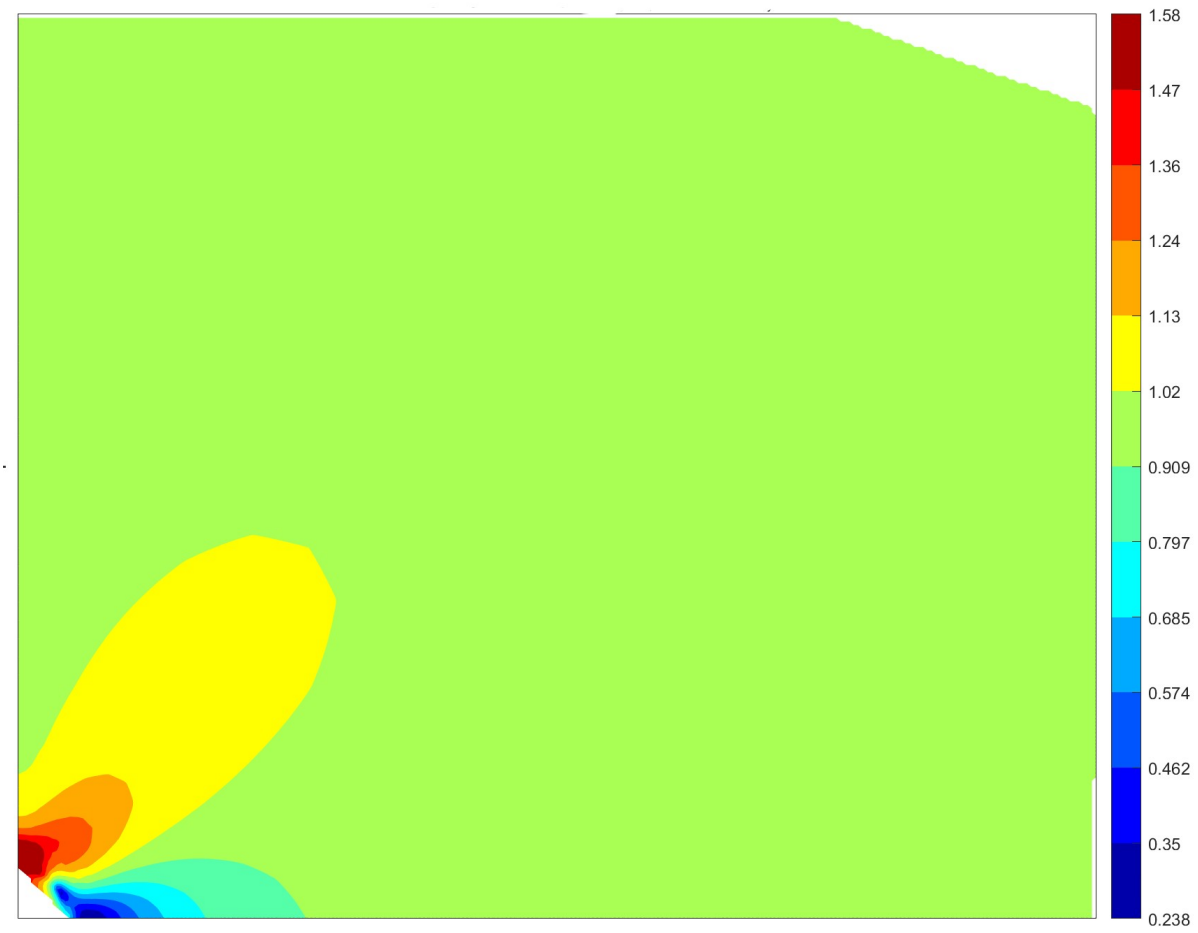

Figure 7.3: Von Mises SCF for plate with elastic-plastic material definition - applied stress 481 MPa

7.3. Validation

Due to the limited experimental data available near the vicinity of the hole during the tensile tests of the perforated specimens, the analytical model is compared to the FEA in addition to the few DIC data points available. The comparisons are performed at the location of maximum stress on the plate under uniaxial tension - location marked by the white line in Figure 7.4. The DIC taken at the load time of crack initiation at the edge of the hole during a tensile test of the perforated specimens is shown in Figure 7.4. Figure 7.5 shows the distribution of hoop stress concentration factors for the analytical solution method with and without prestrain.

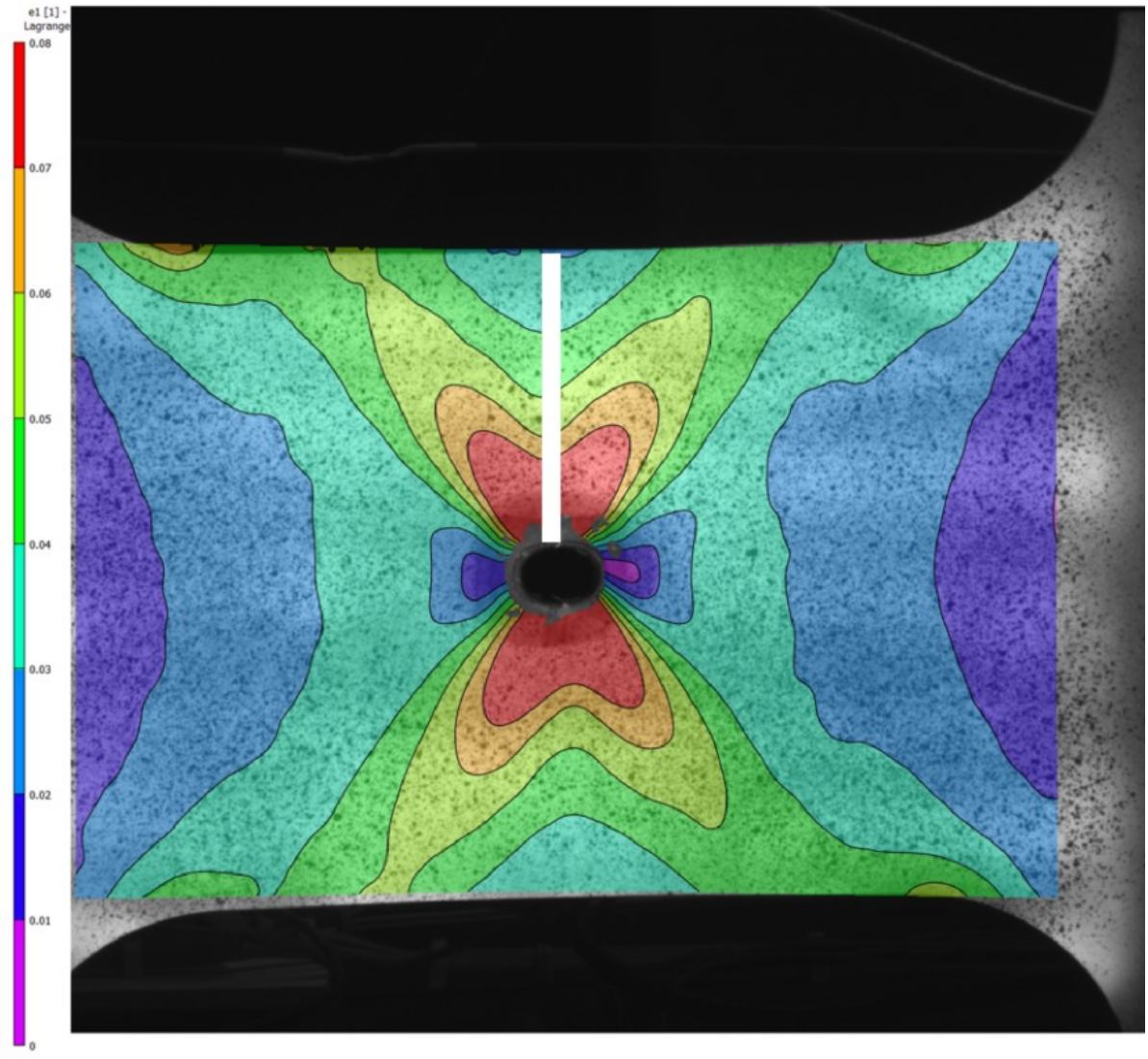

Figure 7.4: EH-RD1 DIC at uniaxial load of crack initiation (applied stress of 481 MPa)

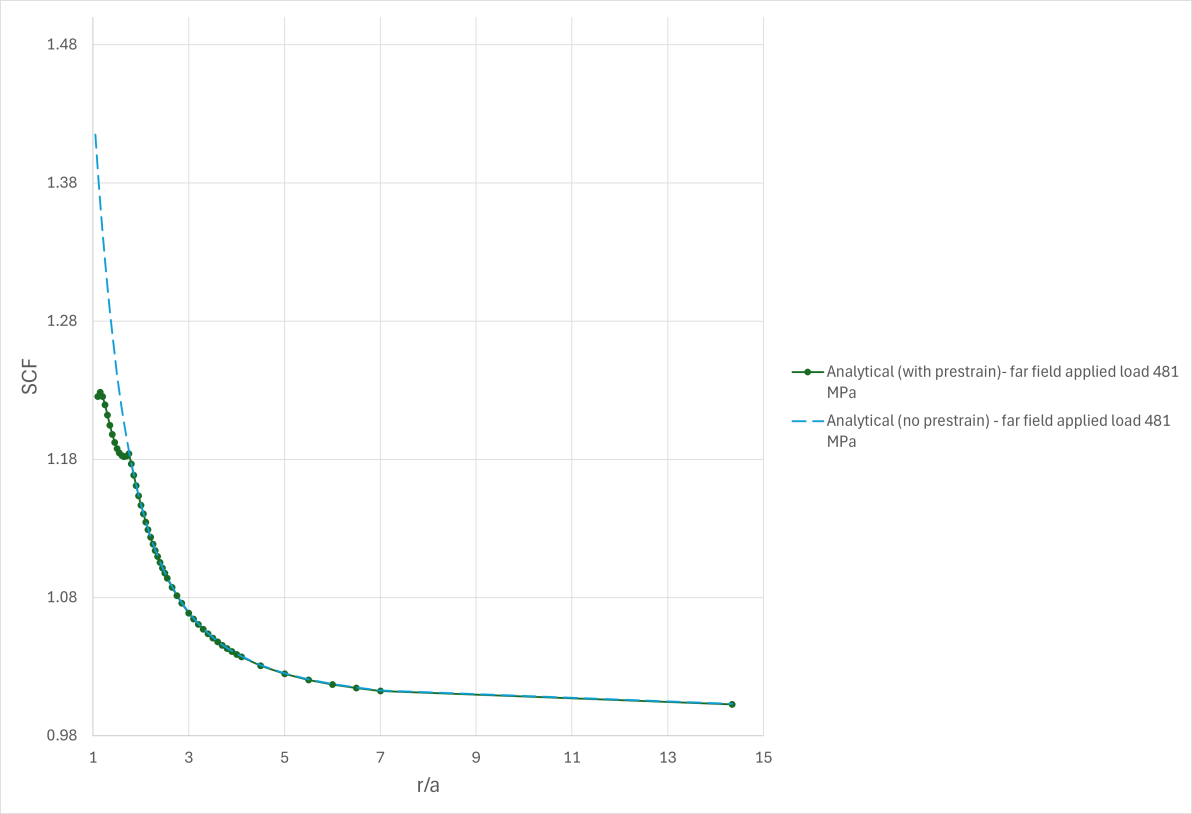

Figure 7.5: Hoop stress SCF at θ = 90 degrees for far field applied stress 481 MPa

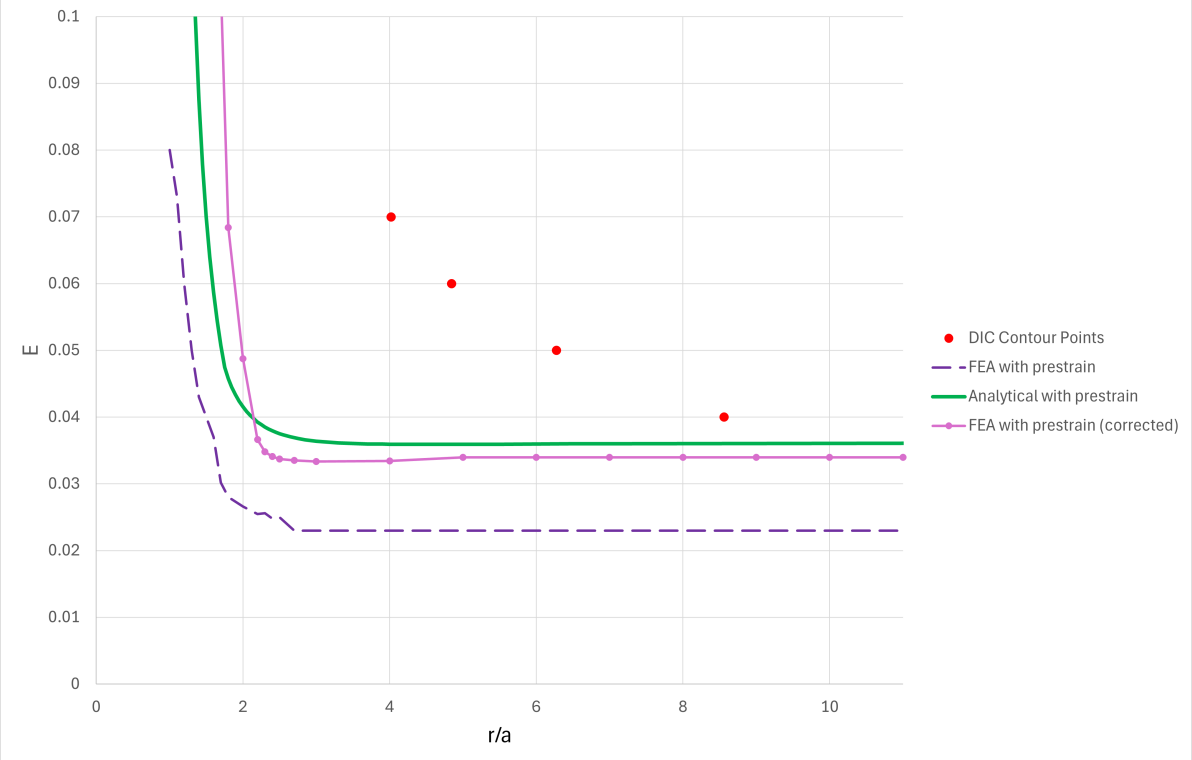

Figure 7.6: Comparison of the first principal strain at θ = 90 degrees for far field applied stress 481 MPa

8

Discussion and Recommendations

8.1. Discussion

In a plate of elastic material under uniaxial tension with a discontinuity, the plastic zone at the discontinuity begins forming when the local stress at the edge reaches the yield stress. The relationship between the local stress at the edge of the discontinuity to the stress at a far field location in the plate (the SCF) informs us on the point in loading time at which yielding begins at the discontinuity. For purely elastic materials, the SCF at the hole edge is theoretically equal to 3, as predicted by Kirsch's solution for a circular hole in an infinite plate.

With Stowell's method, Kirsch's solution is scaled by the secant modulus factor that ties the material properties to the stress field, introducing effects of plasticity. The analytical method with no prestrain included results in a reduced SCF of 1.4, including prestrain in the method results in a further reduction of the SCF by approximately 15.7% (Figure 7.5). This is expected because the numerator of the scaling secant modulus ratio increases with the prestrain incorporated.

Comparison with the DIC data points shows an offset between the the principal Green–Lagrange strain, however strong conclusions cannot be drawn from the lack of data. At an r/a of approximately 8.6 we can see the analytical method with prestrain results in a strain of 0.036 which is near the DIC value of 0.04. The offset between the strain curves from the analytical and FEA methods suggest that the material definitions used for the hardened material zones may not be substantial enough.

8.2. Relevance

The relevance of this thesis lies in its contribution to the understanding and prediction of structural behavior in pre-damaged high-strength steel components, specifically those subjected to ballistic perforation. In real-world applications (such as naval vessels) structural elements are at risk of exposure to high-energy impacts that leave behind localized damage zones. Assessing the residual strength and risk of further failure of these components is critical for making informed decisions about repair, continued use, or decommissioning. Advancing methods to estimate the relationship between the stress concentration at the damage and the far field stress of a plate-like structural component (such as a vessel bulkhead) enables increased efficiency in engineering evaluations.

Traditional analytical models for circular cutouts in a plate often assume undamaged, homogeneous material behavior, while numerical models capable of capturing post-damage effects can be computationally intensive and require detailed calibration. This thesis begins to address this gap by introducing a semi-analytical model that incorporates prestrain effects and strain hardening behavior based on measurable physical properties (Vickers hardness). In the context of future technologies and structural resilience, this work contributes to a broader effort to design with damage tolerance in mind and to develop frameworks that account for material history.

8.3. Limitations

While this thesis introduces a novel and efficient framework for modeling the stress and strain behavior of prestrained, ballistically-perforated steel plates, several limitations should be acknowledged that constrain the application of the current approach.

Assumption of Isotropic Material Behavior

The analytical model assumes that the material is isotropic and that strain hardening occurs uniformly in all directions. In reality, some steels may exhibit anisotropic behavior due to microstructural characteristics, manufacturing processes, or localized deformation patterns. This simplification may lead to under or overestimation of stresses and strains in specific directions, especially in the presence of directional hardening.

Idealized Prestrain Distribution

The prestrain field around the perforation is represented using an exponentially decaying function, calibrated from hardness measurements. While this captures the general trend of strain hardening around the hole, it assumes radial symmetry and smooth transitions, which may not fully reflect the complex and irregular deformation patterns caused by high-velocity impacts (e.g., petaling, mounding, or localized shear bands).

Simplified Geometry and Loading Conditions

The model assumes an infinite plate under uniaxial in-plane loading, which neglects finite boundary effects, erratic thickness variation, and out-of-plane or transverse stresses. These assumptions allow for analytical tractability but limit the accuracy when applied to real structures, especially when perforation occurs near edges, supports, or under multiaxial loading conditions.

Explicit Damage or Fracture Modeling

While the model accounts for prestrain and hardening effects, it does not incorporate damage evolution, void nucleation, or fracture mechanics directly. The approach assumes the material remains continuous and deformable beyond yield, which may not be valid in regions close to fracture initiation or crack propagation. This limits the ability to predict fracture location or crack growth with high accuracy.

Numerical Averaging in Finite Element Implementation

The use of discrete field definitions in Abaqus introduces interpolation-based averaging of material behavior across elements. Since material properties are defined at nodes, the behavior at integration points within elements is an interpolation of multiple stress–strain curves, which may smooth out sharp material transitions and introduce approximation in regions with steep gradients in prestrain.

Limited Experimental Validation

The prestrain distribution and material calibration are based on hardness and tensile test data from a single steel type and a limited set of impact and loading conditions. Broader experimental validation across different materials, geometries, and loading scenarios is necessary to confirm the general applicability of the model.

8.4. Recommendations

To further expand this research, additional steel types should be studied using this framework. Expansion to include more extreme local damage types would also broaden the applicability of this work. To further extend the applicability and robustness of this framework, the following recommendations are proposed:

Further Experimentation on Strain Hardened EH36

Limited experimental data is available to validate the analytical model for the zone of hardened material around the perforation. To close this gap, it is recommended a focused experimental program be performed that is designed to (i) measure the spatial distribution of prior plastic strain $\varepsilon_{p0}(r, \theta)$, (ii) extract local flow parameters $K(r, \theta)$ and $n(r, \theta)$ for the Hollomon/Swift laws, (iii) quantify residual stress fields $\sigma_r(r, \theta)$ and $\sigma_\theta(r, \theta)$, and (iv) document damage features (voids, shear bands, porosity) that correlate with crack initiation. The methods below are chosen to be complementary in spatial resolution, and depth sensitivity.

Multi-scale field mapping:

- Micro-Vickers hardness mapping (HV0.1–HV1). Perform a dense grid (100–250 m pitch) from the hole edge to $\sim$ 8–12 D along at least four azimuths. Convert HV to a local proxy for flow strength to obtain a first-pass $\varepsilon_{p0}(r, \theta)$ map. Use polished cross-sections ($\leq$ 1 m finish) and report confidence intervals accounting for indentation size effects.
- 3D profilometry of the lip. Confocal or white-light interferometry of the perforation lip records mounding geometry, which is a surrogate for plastic work and helps set accurate boundary geometry for FEM validation.
- Residual stress (XRD, $\sin^2\psi$). Map σ_r, σ_θ along radial paths at 0.25–0.5 mm steps. Repeat after controlled electrolytic layer removal to estimate near-surface gradients.
- EBSD on radial cross-sections. Kernel average misorientation (KAM) provides a geometrically necessary dislocation (GND) density proxy and thus a qualitative ε_{p0} indicator. Examine multiple azimuths (0°, 90°, 180°, 270°) to capture anisotropy.

Local constitutive response:

- Instrumented/spherical indentation (CSM). Use multiple indenter radii (20–100 m) and inverse analysis to extract local E, yield, and K, n at selected r/a values; include unload–reload segments to sense kinematic hardening (Bauschinger) effects.
- Miniature tensile & shear-punch tests. Wire-EDM sub-size dogbones or ∅ 3–6 mm shear-punch coupons lifted from annular bands (e.g., $r/a = 1.1, 1.3, 1.5, \ldots$) provide true stress–strain curves and ductility versus distance from the hole, anchoring the hardness/indentation conversions.

High-resolution reloading fields:

- In-situ SEM micro-DIC. Using a micro-tensile stage, perform gentle reloading (to $\sim$ 10–20% of global yield) with 0.1–2 m spatial resolution to capture near-edge strain gradients that macro-DIC misses. These fields directly validate the Stowell-based stress/strain predictions in the annulus of interest.
- Through-thickness residual stress. Neutron diffraction or layer-removal XRD provides depth-resolved σ_r, σ_θ for 3D validation.

Damage characterization:

- Micro-CT of the lip region. Quantify void/crack populations and porosity around the rim; correlate with EBSD and hardness bands and with predicted hot-spots.
- Site-specific TEM (FIB lift-outs). Examine dislocation substructures, shear band thickness, and precipitate/crack interactions to support the chosen hardening law and help explain anisotropy in crack initiation.

Apply Framework to Additional Materials

The current study focuses on EH36 steel, which is representative of high-strength structural steels used in maritime applications. Future work should apply the developed analytical-numerical framework to other steel types (e.g., S690, S960, or dual-phase steels) and potentially to aluminum or titanium alloys. This would test the broader applicaiton potential of the model and identify material-dependent behaviors related to strain hardening, ductility loss, and prestrain gradient formation.

Investigate More Severe Damage Geometries

While this work models damage based on a near-cylindrical ballistic perforation, real-world impacts may produce more severe local deformation, such as mounding, petaling, or shear plugging. Future research should incorporate these more complex geometries to evaluate how non-axisymmetric or irregular deformation shapes affect the local stress and strain fields, particularly under further loading.

Incorporate Out-of-Plane and Multiaxial Loading

The current analysis is limited to in-plane uniaxial tension following the perforation event. Future investigations should include out-of-plane loading conditions, such as bending or pressure-induced bulging, which are common in structural and naval contexts. Multiaxial stress states would require adaptations of the stress field model and may necessitate use of alternative or more advanced yield criteria (e.g., Hill, Barlat).

Extend to Anisotropic and Directionally Hardened Materials

This thesis assumes isotropic material behavior and isotropic hardening. Many steels—especially those rolled or cold-worked—exhibit anisotropic mechanical properties and directional strain hardening. Future work should incorporate anisotropic yield criteria and hardening models (e.g., Hill's criterion or distortional hardening approaches) to more accurately model directional behavior in real materials.

Include Finite Plate Boundary Effects

The analytical model assumes an infinite or semi-infinite plate, which simplifies the derivation but may not reflect actual structural configurations. Incorporating finite boundary conditions—either analytically or via parametric FEM studies—would help assess how boundary proximity affects stress redistribution and failure progression. This would be particularly important for smaller panels or components with nearby supports, cutouts, or geometric constraints.

9

Conclusion

This thesis developed an analytical and numerical framework to model the stress field in high-strength steel plates containing a ballistically-induced perforation, with a focus on the influence of prestrain near the perforation on the SCF. Existing models, including Stowell's plasticity-corrected stress concentration approach and strain hardening laws such as Hollomon and Swift, were evaluated and extended to attempt to account for the residual plastic deformation introduced during ballistic impact.

A modified version of Stowell's analytical solution was proposed, incorporating a spatially varying prestrain field derived from Vickers hardness measurements. The stress field under uniaxial, far field tension was defined using a Stowell formulation modified with a Swift style hardening law that included the prestrain field. The results shows a gap still exists between the proposed semi-analytical model and the physics occurring under new loading at the location of prior damage in a plate. The resultant SCF of the analytical method with prestrain is lower than the SCF derived from Stowell's original method without prestrain, however additional validation is required to confirm this holds for more than one material.

This work demonstrates that incorporating hardness-estimated prestrain effects into Stowell's analytical stress field model lowers the SCF at the location of existing damage. Further research into additional methods of quantifying prestrain and expansion of this framework to include additional material types, damage geometries, and loading conditions will enable broader validation of the model's applicability and support its use in structural integrity assessments for impact-damaged steel components.

Bibliography

[1] A. P. Boresi and R. J. Schmidt. *Advanced mechanics of materials*. 6th. Wiley, 2002, p. 704. ISBN: 978-0-471-43881-6.

[2] M. J. Buehler and T. Ackbarow. “Materials Today”. In: *Materials Today* 10.9 (2007). Image adapted from Buehler, M. J., & Ackbarow, T., Materials Today, 10(9), 46-58, 2007. Reproduced with permission requested. Annotations added by the author., pp. 46–58.

[3] W. Callister. *Materials Science and Engineering*. John Wiley Sons, Inc., 1951.

[4] B.-Q. Chen, B. Liu, and C. Guedes Soares. “Experimental and numerical investigation on a double hull structure subject to collision”. In: *Ocean Engineering* 256 (July 2022), p. 111437.

[5] G. Cowper and P. S. Symonds. “Strain-hardening and strain-rate effects in the impact loading of cantilever beams”. In: *Proceedings of the 1st U.S. National Congress of Applied Mechanics*. 1957, pp. 68–72. URL: https://api.semanticscholar.org/CorpusID:135389032.

[6] R. Hill. *The mathematical theory of plasticity*. Oxford, U.K.: Oxford University Press, 1950.

[7] A. Hirano, M. Sakane, and N. Hamada. “Relationship between Vickers Hardness and Inelastic Material Constants”. In: *Journal of the Society of Materials Science, Japan* (2007).

[8] J. H. Hollomon. “Tensile deformation”. In: *Transactions of the AIME* 162 (1945), pp. 268–290.

[9] G. R. Irwin. “Plastic zone near a crack and fracture toughness”. In: *Sagamore Research Conference Proceedings*. Vol. 4. Syracuse, NY, 1961, pp. 63–78.

[10] G. R. Johnson and W. H. Cook. “A constitutive model and data for metals subjected to large strains, high strain rates, and high temperatures”. In: *Proceedings of the 7th International Symposium on Ballistics*. Vol. 21. 1. The Hague, Netherlands: International Ballistics Committee, 1983, pp. 541–547.

[11] G. Kirsch. “Die Theorie der Elastizität und die Bedürfnisse der Festigkeitslehre”. In: *Zeitschrift des Vereines Deutscher Ingenieure* 42 (1898), pp. 797–807.

[12] S. Kouzoudis. “Failure micro-mechanisms of EH-36 High Strength Low Alloy Steels after ballistic impact”. Master’s thesis. Technische Universiteit Delft: Delft University of Technology, 2024.

[13] S. Kouzoudis. *Fragment damage: Evaluation of microstructure and internal stresses*. Technical Report. Supervisors: Dr. V. Popovich, Dr. V. Bertolo, Andre van Erkel (TNO). Delft University of Technology, Dec. 2023.

[14] R. Von Mises. “Mechanik der festen Körper im plastisch-deformablen Zustand”. In: *Göttin. Nachr. Math. Phys.* (1913), pp. 582–592.

[15] H. Neuber. “Theory of stress concentration for shear-strained prismatic bodies with arbitrary nonlinear stress-strain law”. In: *Journal of Applied Mechanics* 28 (1961), pp. 544–550.

[16] R. K. Nutor, N. K. Adomako, and Y. Z. Fang. “Using the Hollomon model to predict strain-hardening in metals”. In: *American Journal of Materials Synthesis and Processing* 2.1 (2017), pp. 1–4. DOI: 10.11648/j.ajmsp.20170201.11. URL: http://www.sciencepublishinggroup.com/j/ajmsp.

[17] Siemen F.P.M. Obers et al. “The effect of the yield to tensile strength ratio on stress/strain concentrations around holes in high-strength steels”. In: *Marine Structures* 84 (2022), p. 103205.

[18] A. G. Odeshi, S. Al-Ameeri, and M. N. Bassim. “Effect of strain rate on plastic deformation of a low alloy steel subjected to ballistic impact”. In: *Journal of Materials Processing Technology* 162-163 (May 2005), pp. 385–391.

[19] E.J. Pavlina and C.J. Van Tyne. *Correlation of Yield Strength and Tensile Strength with Hardness for Steels*. Tech. rep. ASM International, 2008.

[20] L. L. Pije. “The failure behaviour of steel bulkheads: A numerical study on the failure of steel bulkheads exposed to a combination of fragment spray and blast loading”. Thesis committee: Prof. Dr. L. J. Sluys, Dr. C. L. Walters, W. J. Wong, O. J. Coppejans. Master’s thesis. Delft, Netherlands: Delft University of Technology, Feb. 2022. URL: https://repository.tudelft.nl/.

[21] A. R. Prabowo et al. “On the failure behaviour to striking bow penetration of impacted marine-steel structures”. In: *Curved and Layered Structures* 5.1 (2018), pp. 68–79. DOI: 10.1515/cls-2018-0006.

[22] F. Pursche and L. W. Meyer. “Correlation between dynamic material behavior and adiabatic shear phenomenon for quenched and tempered steels”. In: *Engineering Transactions* 59.2 (2011), pp. 67–84.

[23] J. P. Riegel and D. Davison. “Consistent constitutive modeling of metallic target penetration using empirical, analytical, and numerical penetration models”. In: *Defence Technology* 12.2 (2016), pp. 201–213. DOI: 10.1016/j.dt.2015.11.006. URL: https://www.sciencedirect.com/science/article/pii/S221491471500080X.

[24] Z. Rosenberg and E. Dekel. *Terminal ballistics*. 2nd. Singapore: Springer, 2016. ISBN: 978-981-10-0393-6. DOI: 10.1007/978-981-10-0395-0.

[25] S. Sen, A. Shaw, and S. Nayak. “A mathematical model for perforation of metal plates through adiabatic shear plugging”. In: *International Journal of Impact Engineering* 163 (2022). Department of Civil and Environmental Engineering, Birla Institute of Technology, Mesra, Ranchi, India; Department of Civil Engineering, Indian Institute of Technology Kharagpur, India; Structural Division, ZURU Tech India Pvt Ltd, India., p. 104175.

[26] M. Storheim and J. Amdahl. “On the sensitivity to work hardening and strain-rate effects in nonlinear FEM analysis of ship collisions”. In: *Ships and Offshore Structures* (Jan. 2017).

[27] E. Z. Stowell. “Stress and strain concentration at a circular hole in an infinite plate”. In: *NACA Report* (1950).

[28] H. W. Swift. “Plastic instability under plane stress”. In: *Journal of the Mechanics and Physics of Solids* 1 (1952), pp. 1–18.

[29] D. Tabor. *The Hardness of Metals*. Oxford University Press, 1951.

[30] T. Wierzbicki. *Structural Mechanics*. Massachusetts Institute of Technology, LibreTexts, 2024.

[31] T. T. Yu and P. Liu. “Improved implementation of the extended finite element method for stress analysis around cracks”. In: *Archives of Civil and Mechanical Engineering* 11.3 (2011), pp. 787–805.

[32] F. J. Zerilli. “Dislocation mechanics-based constitutive equations”. In: *Metallurgical and Materials Transactions A* 35 (2004), pp. 2547–2555. DOI: 10.1007/s11661-004-0201-x. URL: https://doi.org/10.1007/s11661-004-0201-x.

[33] Z. Zhang et al. “Prestrain History Effect on Ductile Fracture of Pipeline Steels”. In: *International Seminar on Application of High Strength Line Pipe and Integrity Assessment of Pipeline*. 2006.

A

Code

```
%% ============================
% File: stowell_eps_sol.m
% Returns ep field, smoothed prestrain profile used
%% ============================

function [eps_sol, eps_pre, iters] = stowell_eps_sol(r_vec, theta_vec, yield_csv, E, K, n,
    sigma_inf, a, Es_inf)
% STOWELL_EPS_SOL
%   Solve for the incremental equivalent plastic strain ep(r ,) using 'Stowells field and
    shifted Hollomon law
%
% Inputs:
%   r_vec       [N×1] radii (mm)
%   theta_vec   [1×M] angles (rad)
%   yield_csv   CSV with column 'Eps_pre' giving prestrain vs r
%   E '          Youngs modulus (MPa)
%   K, n        Hollomon parameters (MPa, -)
%   sigma_inf   remote (far-field) (MPa)
%   a           hole radius (mm)
%   Es_inf      far-field secant modulus
%
% Output:
%   eps_sol     [N×M] incremental equivalent plastic strain ep(r ,)   0
%   eps_pre     [N×1] smoothed, baseline-corrected prestrain profile used
%   iters       [N×M] iteration counts (diagnostic)


  % Prestrain profile (scalar eq. plastic prestrain vs r)
  T = readtable(yield_csv);
  if ~ismember('Eps_pre', T.Properties.VariableNames)
      error('CSV must contain column named Eps_pre.');
  end
  eps_pre_fun = fit_prestrain_function(r_vec, T.Eps_pre(:), a);
  eps_pre     = eps_pre_fun(r_vec);

  N = numel(r_vec);  M = numel(theta_vec);
  eps_sol = zeros(N, M);
  iters   = zeros(N, M);

  % solver settings
  damp  = 0.7;     % damping factor for secant step (0<damp<=1)
  tolX  = 1e-10;   % strain increment tolerance
  tolF  = 1e-6;    % residual tolerance in MPa
  maxIt = 60;      % max iterations

  % Neighbor continuation improves smoothness & speed
  use_continuation = true;

  % loop over grid points
```

```
  for i = 1:N
      r   = r_vec(i);
      ep0 = eps_pre(i);

      for j = 1:M
          th = theta_vec(j);


          % Residual: f(ep) = sigma_eq(ep) - K*(ep0+ep)^n
          resid = @(ep) vmises_stowell(ep, ep0, r, th, E, K, n, sigma_inf, a, Es_inf) ...
                        - K*(ep0 + (ep)).^n;

          % Seed near the far-field plastic increment at this radius
          ep_seed = ((sigma_inf/K)^(1/n) - ep0);
          if use_continuation
              if j > 1, ep_seed = 0.5*ep_seed + 0.5*eps_sol(i,j-1); end
              if i > 1, ep_seed = 0.5*ep_seed + 0.5*eps_sol(i-1,j); end
              ep_seed = (ep_seed);
          end

          % Two nearby secant guesses
          ep0g = ep_seed;
          ep1g = max(ep_seed + max(1e-6, 0.2*ep_seed), 1e-8);

          f0 = resid(max(ep0g,0));
          f1 = resid(max(ep1g,0));

          % Projected, damped secant iterations
          ep  = ep1g;  dmp = damp;  it = 0;
          for it = 1:maxIt
              denom = (f1 - f0);
              if abs(denom) < 1e-20
                  step = 0.1*max(1e-6, ep1g);
              else
                  step = - f1 * (ep1g - ep0g) / denom;
              end

              ep2 = max(ep1g + dmp*step, 0);
              f2  = resid(ep2);

              % Convergence tests
              if abs(f2) < tolF || abs(ep2 - ep1g) < tolX
                  ep = ep2; break;
              end

              % Update secant history
              ep0g = ep1g;  f0 = f1;
              ep1g = ep2;   f1 = f2;

              % Damping back-off if progress slow
              if it > 8 && sign(f1) == sign(f0)
                  dmp = 0.5*dmp;
              end
          end

          if it == maxIt
              ep = ep2;  % best effort at exit
          end

          eps_sol(i,j) = ep;      % already   0 by projection
          iters(i,j)   = it;
      end
  end
end


% Helper: von Mises stress under Stowell with Es_loc/Es_inf.
% Plane-stress VM formula
function s_vm = vmises_stowell(ep, ep0, r, th, E, K, n, sigma_inf, a, Es_inf)
  ep_eff      = max(ep, 0);        % enforce ep   0 in evaluation
  ep_tot      = ep0 + ep_eff;      % total equiv. plastic at point
```

```
  sigma_loc   = K * (ep_tot)^n;    % Hollomon stress at current state
  eps_tot_loc = sigma_loc/E + ep_tot;      % total true strain
  Es_loc      = sigma_loc / eps_tot_loc;   % local secant modulus

  c2 = cos(2*th); rr2 = (a/r)^2; rr4 = rr2^2; fac = (Es_loc/Es_inf);

  sig_th = 0.5*sigma_inf*( 1 + rr2 - fac*(1+3*rr4)*c2 );
  sig_r  = 0.5*sigma_inf*( 1 - rr2 + fac*(1-4*rr2+3*rr4)*c2 );
  tau_rt = -0.5*sigma_inf*fac*(1+2*rr2-3*rr4)*sin(2*th);

  % Plane-stress von Mises (includes shear)
  s_vm = sqrt( sig_r.^2 - sig_r.*sig_th + sig_th.^2 + 3*tau_rt.^2 );
end
```

```
%% ============================
% File: recompute_stresses.m using Stowell + shifted Hollomon

clear; clc; close all;

%% 1) Define geometry, material, and loading
% Radial positions (match yield_results.csv Radius_mm)
r_vec = [10.484, 10.999, 11.499, 11.999, 12.499, 12.999, 13.499, ...
         13.999, 14.499, 14.999, 15.485, 15.999, 16.486, 16.985, ...
         17.499, 17.999, 18.477, 18.981, 19.499, 19.999, 20.499, ...
         20.999, 21.482, 21.999, 22.499, 22.999, 23.496, 23.999, ...
         24.499, 24.999, 25.499, 26.500, 27.500, 28.500, 30.000, ...
         31.000, 32.000, 33.000, 34.000, 35.000, 36.000, 37.000, ...
         38.000, 39.000, 40.000, 41.000, 45.000, 50.000, 55.000, ...
         60.000, 65.000, 70.000, 143.46];    % [mm]

% No duplicate endpoint at 2
theta_vec  = linspace(0,2*pi,361);
theta_vec(end) = [];

yield_csv  = 'yield_results_r4.csv';

K          = 921.94;        % Hollomon K [MPa]
n          = 0.189982;      % hardening exponent
E          = 202366.9202;   % Young's modulus [MPa]
sigma_inf  = 481;           % far-field axial Cauchy stress [MPa]
a          = 10;            % hole radius [mm]
nu         = 0.30;          % Poisson's ratio

%% 2) Solve for the -equivalentplastic strain field
ep0_inf    = 0; % usually zero far from the hole
ep_inf     = max((sigma_inf/K)^(1/n) - ep0_inf, 0);
eps_tot_inf = sigma_inf/E + ep_inf;
E_s_inf    = sigma_inf / eps_tot_inf;
% Solve ep(r ,); also returns smoothed prestrain profile used internally
[eps_sol, eps_pre_vec, iters] = stowell_eps_sol(r_vec, theta_vec, yield_csv, E, K, n,
    sigma_inf, a, E_s_inf);

%% 3) Allocate arrays
N = numel(r_vec);
M = numel(theta_vec);
sigma_theta   = zeros(N,M);
sigma_r       = zeros(N,M);
tau_rtheta    = zeros(N,M);
von_mises     = zeros(N,M);
e1_lagrangian = zeros(N,M);
e2_lagrangian = zeros(N,M);

%% 4) Recompute Stowell stress field using eps_sol
for i = 1:N
  % Guard near-hole radius to avoid roundoff in (a/r)^2
  r = max(r_vec(i), a*(1+1e-8));

  for j = 1:M
    th = theta_vec(j);

    %local secant modulus (shifted Hollomon, based on TOTAL plastic)
```

```
    eps_p_tot_loc = eps_sol(i,j) + eps_pre_vec(i);   % total plastic at (r ,)
    sigma_loc     = K * (eps_p_tot_loc)^n;           % true stress from Hollomon
    eps_tot_loc   = sigma_loc/E + eps_p_tot_loc;     % total true strain
    E_s_loc       = sigma_loc / eps_tot_loc;

    % Stowell field
    c2   = cos(2*th);
    rr2  = (a/r)^2;    rr4 = rr2^2;
    fac  = (E_s_loc/E_s_inf);

    sigma_theta(i,j) = 0.5*sigma_inf * ( 1 + rr2 - fac*(1+3*rr4)*c2 );
    sigma_r(i,j)     = 0.5*sigma_inf * ( 1 - rr2 + fac*(1-4*rr2+3*rr4)*c2 );
    tau_rtheta(i,j)  = -0.5*sigma_inf * fac * (1 + 2*rr2 - 3*rr4) * sin(2*th);

    % Von Mises (plane stress)
    von_mises(i,j) = sqrt( sigma_r(i,j)^2 - sigma_r(i,j)*sigma_theta(i,j) ...
                         + sigma_theta(i,j)^2 + 3*tau_rtheta(i,j)^2 );

    % Principal stresses from current state
    sigma_avg = 0.5*(sigma_r(i,j) + sigma_theta(i,j));
    Rmohr     = sqrt( ((sigma_r(i,j) - sigma_theta(i,j))/2)^2 + tau_rtheta(i,j)^2 );
    s1 = sigma_avg + Rmohr;   % max principal stress
    s2 = sigma_avg - Rmohr;   % min principal stress

    % Deviatoric principal stresses and J2 equivalent
    sig_m = (s1 + s2) / 3;        % plane stress => s3 = 0, mean based on 3 comps
    t1 = s1 - sig_m;
    t2 = s2 - sig_m;
    t3 = - (t1 + t2);
    sigma_eq = sqrt(1.5*(t1^2 + t2^2 + t3^2));
    sigma_eq = max(sigma_eq, 1e-9*max(1, sigma_inf));  % floor

    % TOTAL equivalent plastic strain at this point
    ep_bar_tot = eps_pre_vec(i) + max(eps_sol(i,j), 0);

    % Plastic principal TRUE strains (associated flow, proportional to deviatoric)
    epsp1_true = (3/2)*(t1/sigma_eq) * ep_bar_tot;
    epsp2_true = (3/2)*(t2/sigma_eq) * ep_bar_tot;
    % epsp3_true = (3/2)*(t3/sigma_eq) * ep_bar_tot;

    % Elastic TRUE principal strains (Hooke, plane stress)
    epse1_true = (s1 - nu*s2)/E;
    epse2_true = (s2 - nu*s1)/E;

    % TOTAL TRUE principal strains
    eps1_true_tot = epse1_true + epsp1_true;
    eps2_true_tot = epse2_true + epsp2_true;

    % Convert principal TRUE → GreenLagrange
    e1_lagrangian(i,j) = 0.5*(exp(2*eps1_true_tot) - 1);
    e2_lagrangian(i,j) = 0.5*(exp(2*eps2_true_tot) - 1);

  end
end

%% 5) Plots
r_norm = (r_vec)/ a;                    % center-based radii, normalized
[~, j90] = min(abs(theta_vec - pi/2));

figure; plot(r_norm, von_mises(:,j90), 'o-','LineWidth',1.5);
xlabel('r / a'); ylabel('\sigma_{vm} (MPa)');
title('Von Mises stress at \theta = \pi/2 vs. r/a'); grid on;

% Experimental -firstprincipal strain data (example placeholders)
r_data_mm   = [39.25, 49.99, 68.59, 98.28, 133.46];  % mm (distance from hole edge)
e1_data_eng = [0.07, 0.06, 0.05, 0.04, 0.03];        % engineering strain

% Convert to GL and normalize radii (edge-based → center-based by +a)
e1_data_GL  = e1_data_eng + 0.5*e1_data_eng.^2;
r_data_norm = (r_data_mm + a) ./ a;

```

```
figure; hold on;
plot(r_norm, e1_lagrangian(:,j90), 's-','LineWidth',1.5, 'DisplayName','Analytical E_1');
% plot(r_norm, e2_lagrangian(:,j90), '^-','LineWidth',1.5, 'DisplayName','Analytical E_2');
plot(r_data_norm, e1_data_GL,'s','LineWidth',1.5,'DisplayName','Experimental E_1 (GL)');
hold off;
xlabel('r / a');
ylabel('Principal -GreenLagrange strain');
title('Principal -GreenLagrange strains at \theta = \pi/2 vs. r/a');
grid on;
ylow = min(min(e2_lagrangian(:,j90)) - 0.01, 0);
ylim([0 0.1]);

% Contour of E1 (normalized coordinates)
[Theta, R] = meshgrid(theta_vec, r_vec);
X = (R./a) .* cos(Theta);  Y = (R./a) .* sin(Theta);
figure;
contourf(X, Y, e1_lagrangian, 20, 'LineStyle','none');
axis equal tight; box on; grid on;
xlabel('x / a'); ylabel('y / a');
title('Contour of First Lagrangian Strain E_1');
cb = colorbar; cb.Label.String = 'E_1';
clim([0 0.08]);
hold on; th = linspace(0, 2*pi, 361);
plot(cos(th), sin(th), 'k-', 'LineWidth', 1.0); hold off;
set(gcf,'Color','w');

% Hoop stress at   = /2
hoop_raw = sigma_theta(:, j90);
hoop_scf = sigma_theta(:, j90) / sigma_inf;
r_over_a = r_vec(:) / a;

figure;
plot(r_over_a, hoop_raw, 'o-','LineWidth',1.5, 'DisplayName','\sigma_{\theta\theta} (MPa)');
    hold on;
plot(r_over_a, hoop_scf, 's-','LineWidth',1.5, 'DisplayName','\sigma_{\theta\theta}/\sigma_{\
    infty}');
hold off; grid on;
xlabel('r / a');
ylabel('Value');
title('Hoop stress at \theta = \pi/2 vs. r/a');
legend('Location','best');

% Optional: export numeric data
out_hoop = [r_over_a, hoop_raw, hoop_scf];
fname_hoop = 'hoop_theta90.csv';
writematrix(out_hoop, fname_hoop);

%% Quadrant contour: von Mises with Abaqus-like palette (0      /2)
th_mask = (theta_vec >= 0) & (theta_vec <= pi/2 + 1e-12);

[ThetaQ, RQ] = meshgrid(theta_vec(th_mask), r_vec);
Xq = (RQ./a).*cos(ThetaQ);
Yq = (RQ./a).*sin(ThetaQ);
Zq = von_mises(:, th_mask);

normalize_scf = false;
if normalize_scf
    Zplot = Zq / sigma_inf;
    zlabel = '\sigma_{vm} / \sigma_\infty';
else
    Zplot = Zq;
    zlabel = '\sigma_{vm} [MPa]';
end

nLevels = 13;
zmin = min(Zplot(:));  zmax = max(Zplot(:));
levels = linspace(zmin, zmax, nLevels);

figure;
[~,h] = contourf(Xq, Yq, Zplot, levels);
set(h,'LineColor','none');
```

```
axis equal tight; box on; grid on;
xlabel('x␣/␣a'); ylabel('y␣/␣a');
title('\sigma_{vm}:␣Quadrant␣0␣\leq␣\theta␣\leq␣\pi/2');
clim([levels(1) levels(end)]);

colormap(jet(nLevels-1));
cb = colorbar;
cb.Label.String = zlabel;
cb.Ticks = levels;
cb.TickLabels = compose('%+.3e', levels);

hold on; thq = linspace(0, pi/2, 181);
plot(cos(thq), sin(thq), 'k-', 'LineWidth', 1.0); hold off;
set(gcf,'Color','w');

cmap12 = [ ...
    0.00 0.00 0.56
    0.00 0.00 1.00
    0.00 0.50 1.00
    0.00 1.00 1.00
    0.00 1.00 0.50
    0.00 1.00 0.00
    0.50 1.00 0.00
    1.00 1.00 0.00
    1.00 0.80 0.00
    1.00 0.60 0.00
    1.00 0.20 0.00
    1.00 0.00 0.00];
colormap(cmap12);

%% - Quadrant contour: SCF =  _vm /  ϖ_ (0      /2) -
th_mask = (theta_vec >= 0) & (theta_vec <= pi/2 + 1e-12);

[ThetaQ, RQ] = meshgrid(theta_vec(th_mask), r_vec);
Xq = (RQ./a).*cos(ThetaQ);
Yq = (RQ./a).*sin(ThetaQ);
Zscf = von_mises(:, th_mask) / sigma_inf;

nLevels = 13;
use_fixed_range = true;
if use_fixed_range
    zmin = 0.185;
    zmax = 1.581;
else
    zmin = min(Zscf(:));
    zmax = max(Zscf(:));
end
levels = linspace(zmin, zmax, nLevels);

figure;
[~,h] = contourf(Xq, Yq, Zscf, levels);    % no LineColor arg
set(h,'LineColor','none');                 % hide band edges
% set(gcf,'Renderer','painters');          % <- optional: avoids tiny seams in exports
axis equal tight; box on; grid on;
xlabel('x␣/␣a'); ylabel('y␣/␣a');
title('SCF,␣Mises␣(Quadrant␣0␣\leq␣\theta␣\leq␣\pi/2)');
clim([levels(1) levels(end)]);

colormap(jet(nLevels-1));
cb = colorbar;
cb.Label.String = '\sigma_{vm}␣/␣\sigma_{\infty}';
cb.Ticks = levels;
cb.TickLabels = compose('%+.3e', levels);

hold on;
thq = linspace(0, pi/2, 181);
plot(cos(thq), sin(thq), 'k-', 'LineWidth', 1.0);
hold off;

set(gcf,'Color','w');
%% --- Export SCF along theta = 90 deg  (/2) ---
```

```
target_theta = pi/2;
[~, i90] = min(abs(theta_vec - target_theta));
theta90_deg = rad2deg(theta_vec(i90));

% Warn if theta_vec doesn't hit 90° exactly (uses nearest angle)
if abs(theta_vec(i90) - target_theta) > deg2rad(0.1)
    warning('No exact  =90° in theta_vec. Using  =%.6f rad (%.3f°).', ...
            theta_vec(i90), theta90_deg);
end

% SCF = sigma_vm / sigma_inf along that ray (vector over r)
scf_theta90 = von_mises(:, i90) / sigma_inf;
r_over_a    = r_vec(:) / a;

% Two columns: r/a, SCF
out = [r_over_a, scf_theta90];

% Write a simple .scf text file
fname_scf = 'theta90.scf';
fid = fopen(fname_scf,'w');
assert(fid>0, 'Could not open %s for writing.', fname_scf);
fprintf(fid, '%% SCF along theta = 90 deg\n');
fprintf(fid, '%% columns: r_over_a , SCF = sigma_vm/sigma_inf\n');
fprintf(fid, '%% theta_used_deg = %.6f\n', theta90_deg);
fprintf(fid, '%% n = %d\n', numel(r_over_a));
fprintf(fid, '% .10e , % .10e\n', out.');   % r/a, SCF
fclose(fid);

writematrix(out, 'theta90.csv');

%% Quadrant contour: Hoop SCF (0      /2)
th_mask = (theta_vec >= 0) & (theta_vec <= pi/2 + 1e-12);

[ThetaQ, RQ] = meshgrid(theta_vec(th_mask), r_vec);
Xq = (RQ./a).*cos(ThetaQ);
Yq = (RQ./a).*sin(ThetaQ);

Zhoop = sigma_theta(:, th_mask) / sigma_inf;

% Choose contour levels (fixed or data-driven)
nLevels = 13;
use_fixed_range_hoop = false;
if use_fixed_range_hoop
    zmin = 0.0;
    zmax = 3.0;
else
    zmin = min(Zhoop(:));
    zmax = max(Zhoop(:));
end
levels = linspace(zmin, zmax, nLevels);

figure;
[~,h] = contourf(Xq, Yq, Zhoop, levels);
set(h,'LineColor','none');
axis equal tight; box on; grid on;
xlabel('x / a'); ylabel('y / a');
title('Hoop SCF: \sigma_{\theta\theta} / \sigma_{\infty} (0 \leq \theta \leq \pi/2)');
clim([levels(1) levels(end)]);

colormap(jet(nLevels-1));
cb = colorbar;
cb.Label.String = '\sigma_{\theta\theta} / \sigma_{\infty}';
cb.Ticks = levels;
cb.TickLabels = compose('%+.3e', levels);

% Draw the hole edge
hold on; thq = linspace(0, pi/2, 181);
plot(cos(thq), sin(thq), 'k-', 'LineWidth', 1.0);
hold off;

set(gcf,'Color','w');
```